E00-102: Testing the Limits of the Single Particle Model in ^{16}O(e,e′p)

Mattias Andersson
Lund University

Contents

Preface iii

1 Introduction **1**

1.1 Overview 1

1.2 Electron Scattering Framework 3

1.2.1 Inclusive Electron Scattering 3

1.2.2 Semi-Exclusive Electron Scattering 4

1.3 The Impulse Approximation (IA) 7

1.3.1 Plane-Wave IA (PWIA) 7

1.3.2 Distorted-Wave IA (DWIA) 8

1.4 Previous Experimental Work 8

2 Experimental Method **12**

2.1 The Accelerator 12

2.2 Extraction/Hall A 12

2.2.1 Beam Position and Direction 14

2.2.2 Current and Charge Measurements 16

2.2.3 Absolute Energy Measurements 17

2.3 The Target System 19

2.4 The Spectrometers 21

2.4.1 Magnets 21

2.4.2 Collimators 24

2.5 The Detector Package 25

2.5.1 Triggering and Timing 26

2.5.2 Tracking 27

2.5.3 Particle Identification 29

2.6 Data Acquisition 32
2.7 The E00-102 Experiment 32

3 Analysis **35**
3.1 Overview 35
3.2 Calibrations 36
3.3 Yield 42
3.3.1 Determining "Good" Runs 42
3.3.2 Data Reduction Cuts 42
3.3.3 Timing and Coincidence Yield 45
3.3.4 $1p_{1/2}$ State 52
3.4 Cross Section 52
3.4.1 Absolute Cross Section 52
3.4.2 Relative to H(e,e) 52
3.4.3 Phase-Space Normalisation 54
3.4.4 p_{miss}-binning 54
3.4.5 Summary 54

4 Results **58**
4.1 RDWIA Ingredients 58
4.2 Conclusion 60

A MySQL Database **61**

B Diary **63**

C Corrected Yield Error Estimate **65**

D Data subsets **67**

Preface

The contributions made by the author to the this project includes:

- relocating to the Thomas Jefferson National Accelerator Facility located in Newport News, VA, USA, for a period of nine months;
- leading the data acquisition shift work over the forty-day experiment;
- performing "first-pass" analysis tasks including optimising the detector and spectrometer databases;
- creating a database containing all of the information required for normalising the data;
- analysing the "cooked" data to verify its quality and determine for the first time ever the relative probabilities for proton knock-out from the p-shell of ^{16}O at high missing momentum in quasielastic kinematics; and
- authoring this thesis.

Acknowledgments

There are many people I feel gratitude towards.

First of all, my supervisor Dr. Kevin Fissum for inviting me into the project and his incredible patience, invaluable help and support.

Prof. Larry Weinstein at ODU for all his help. The people at JLab that gave me their precious time: Dr. Doug Higinbotham for making me feel welcome at the lab, Dr. Bodo Reitz for valuable discussions on data analysis, Dr. Nilanga Liyanage for providing valuable analysis tools, and Dr. Rikki Roche and Dr. Wendy Hinton for their collaboration. The scientific and support staff in Halla A at JLab for making this work possible.

I would also like to give a special thank you to Prof. Bent Schröder for giving me this opportunity and a lot of support, and to the other people in the Photo-Nuclear Group for their friendship.

Chapter 1

Introduction

This thesis describes a semi-exclusive electron-scattering experiment performed in the autumn of 2001 in Hall A at the Thomas Jefferson National Accelerator Facility (JLab). Electrons were scattered from ^{16}O nuclei provided by a waterfall (H_2O) target and detected in coincidence with knocked-out protons in the Hall A High Resolution Spectrometers (HRS). The purpose of this measurement was to study the $^{16}\mathrm{O}(e,e'p)$ reaction in extreme quasielastic kinematics, thereby testing the limits of the Single-Particle Model.

1.1 Overview

Electron scattering is a powerful tool for the study of the structure and behaviour of nucleons and nuclei. This is because the electromagnetic interaction describing the electron scattering vertex is very well described by the theory of Quantum Electrodynamics (QED)[1]. Further, the electromagnetic interaction is relatively "weak" compared to the hadronic (strong-force) interaction, which allows it to be described with the One-Photon Exchange Approximation (OPEA). The "weakness" of the electromagnetic interaction also means that the virtual exchange photon can sample the entire nuclear volume, in contrast to hadronic probes (protons, for example) that usually interact with only the nuclear surface. Information about the behaviour of the bound-nucleon wave functions in the nuclear interior may thus be obtained.

The greatest advantage of virtual photons over real photons (those with $Q^2 = 0$) is that the energy and 3-momentum of the virtual photon can be varied independently (as long as $Q^2 \equiv \mathbf{q}^2 - \omega^2 \geq 0$)[2], making it possible to selectively probe a wider range of kinematic variables. In particular, this freedom allows for the selection of so-called quasielastic (QE) kinematics (see Section 1.2.1). However, using an electron beam as a probe also has some drawbacks. Since

[1] For example, precision tests have been made for QED predictions for the magnetic moment of the electron. QED predictions agree with the measurement to seven significant figures.

[2] See definitions in Equations 1.2, 1.3 and 1.4. In this text, the convention of letting $c = 1$ and $\hbar = 1$ is followed.

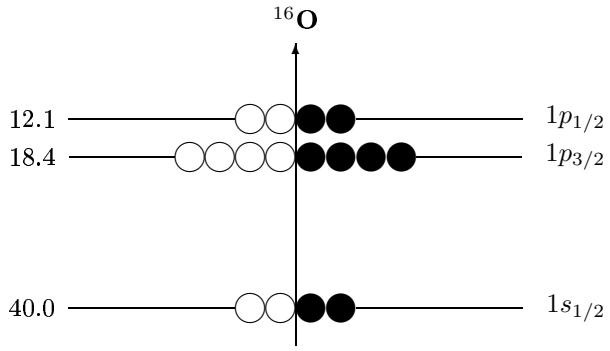

Figure 1.1: Idealised proton and neutron levels in ^{16}O. Protons are represented by empty circles and neutrons by filled circles. The numbers on the left are the separation energies in MeV. On the right are the spectroscopic representations of the quantum numbers for each level.

the electromagnetic interaction is "weak", the reaction cross section[3] is small. To make a statistically significant measurement thus requires high beam intensity and large amounts of beam time. Another difficulty is radiative effects. A high-energy electron radiates photons as it passes through the Coulomb field of a target nucleus. Thus, the simple picture of a single virtual photon being cleanly exchanged (although convenient for describing the reaction theoretically) is always distorted in a real experimental setting, and these distortions must be quantified.

^{16}O is a doubly-magic, closed-shell nucleus. Its bound-nucleon wave functions are relatively easy to calculate. Since proton scattering from ^{16}O has previously been studied in detail [1, 2, 3, 4, 5, 6, 7, 8, 9, 10, 11], the Final-State Interactions (FSI) are in principle well understood[4]. It is therefore possible to make solid theoretical predictions for the cross section. This makes ^{16}O an excellent target for the study of the proton knock-out reaction mechanism. Pure ^{16}O, however, is difficult to handle, as it is highly reactive. The waterfall-target system used for this experiment provided a safe and stable target. Further, whereas the use of other ^{16}O compounds would require additional measurements to subtract the non-^{16}O background, the ^{1}H "contamination" in water can be used for very valuable kinematically overdetermined elastic-scattering measurements.

The measurements in this experiment extend the range of bound-nucleon momenta probed well beyond any previously investigated region in quasielastic kinematics at high momentum transfer (see Section 2.7). Such measurements

[3]The cross section measures the probability for a interaction to occur. The experimental basis for a reaction cross section is the yield, appropriately normalised to take into consideration the properties of the probe and the particle detectors. Thus,

$$\sigma \propto \frac{\text{number of times the reaction occurred}}{(\text{target properties}) \cdot (\text{beam properties}) \cdot (\text{detector properties})}. \tag{1.1}$$

[4]The residual nucleus in the $^{16}\mathrm{O}(e,e'p)$ reaction is ^{15}N, but there are few data for proton scattering from ^{15}N.

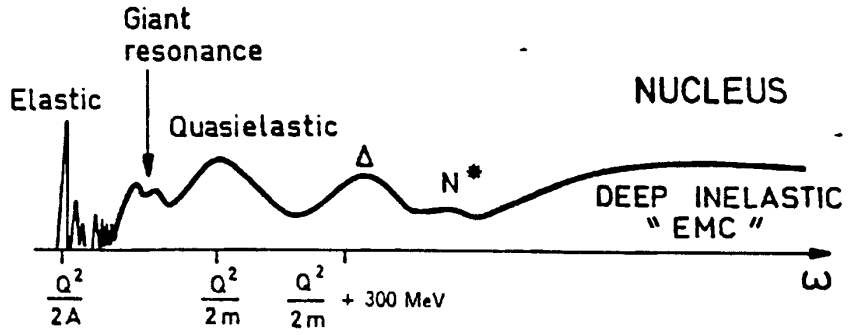

Figure 1.2: Cross-section dependence for inclusive (e, e') as a function of transferred energy ω.

may reveal the limitations of the conventional low-q picture of nuclear structure, which is based on nucleons interacting via meson exchange. This kind of experiment on a heavy nucleus will hopefully expand our understanding of nuclear structure, and simultaneously may provide information on how bound-nucleon properties differ from those of the free nucleon.

1.2 Electron Scattering Framework

1.2.1 Inclusive Electron Scattering

Electron scattering proceeds via the exchange of a virtual photon or photons between the incident electron and the target nucleus. For light- or medium-weight nuclei where $Z\alpha \ll 1$ (where Z is the number of protons and α is the Fine-Structure Constant ($\sim 1/137$)), the electron-scattering process can be approximated by the exchange of a single virtual photon. The virtual exchange photon is characterised by the energy ω and the 3-momentum $\mathbf{q}$ transferred from the electron to the target

$$\omega \equiv E_{\rm i} - E_{\rm f}, \tag{1.2}$$

$$\mathbf{q} \equiv \mathbf{k}_{\rm i} - \mathbf{k}_{\rm f}, \tag{1.3}$$

where $E_{\rm i}$ and $E_{\rm f}$ are the incident and scattered electron energies, respectively, and $\mathbf{k}_{\rm i}$ and $\mathbf{k}_{\rm f}$ are the corresponding electron momenta. The energy transfer ω and the momentum transfer $\mathbf{q}$ are combined to form the 4-momentum $\tilde{q} \equiv (\omega, \mathbf{q})$. More commonly used is Q^2, often defined as $Q^2 \equiv -\tilde{q}^{\,2}$,

$$Q^2 = \mathbf{q}^2 - \omega^2. \tag{1.4}$$

Figure 1.2 illustrates a typical inclusive electron-scattering differential cross section $d^3\sigma/d\Omega_{\rm e} d\omega$ as a function of ω from a nucleus with A nucleons in a single arm (e, e') experiment. From left to right, the first peak is due to elastic scattering from the nucleus, with $\omega = Q^2/2A$ (where A is the mass of the nucleus). The next set of sharp peaks correspond to nuclear excitations into discrete states.

The first of the broad bumps comes from excitation of nuclear collective modes[5]. At $\omega = Q^2/2m$ (where m is the mass of a nucleon), there is a very broad bump called the Quasielastic (QE) Peak. This region corresponds to the virtual photon being absorbed by a single nucleon. In this energy region, the incident electron preferentially interacts with a single target nucleon, and to first approximation the width of the peak can be attributed to the momentum distribution of these target nucleons inside the nucleus. The next two bumps, at higher energy transfer, correspond to the excitation of a nucleon to the Δ and N^* Resonances[6]. The interval between the Quasielastic Peak and the Δ-resonance Peak is called the Dip Region. The area well beyond the N^* resonance is called the Deep-Inelastic Scattering (DIS) Region, where the nucleon resonances overlap into a plateau with no discernible peaks. Here, the electron can be considered to scatter quasielastically from the individual constituent quarks of the nucleon. In this experimental work, the QE scattering region was investigated.

In inclusive electron scattering in the One-Photon Exchange Approximation (or Born Approximation), the virtual photon is completely absorbed by a single nucleon without disturbing the rest of the nucleus. The inclusive differential cross section $d^3\sigma/d\Omega_e d\omega$ can be written

$$\frac{d^3\sigma}{d\Omega_e d\omega} = \sigma_M \left\{ \frac{Q^4}{\mathbf{q}^4} R_L(\omega, Q^2) + \left(\frac{Q^2}{2\mathbf{q}^2} + \tan^2\left(\frac{\theta_e}{2}\right) \right) R_T(\omega, Q^2) \right\}. \quad (1.5)$$

Here, σ_M is the Mott cross section given by

$$\sigma_M \equiv \frac{\alpha^2 \cos^2(\theta_e/2)}{4E_i^2 \sin^4(\theta_e/2)}, \quad (1.6)$$

where E_i is the energy of the incident electron and θ_e is the electron scattering angle with respect to the incident beam direction. The Mott cross section represents scattering from a point target with no structure. The bracketed term allows for the internal structure of the target nucleus. $R_L(\omega, Q^2)$ and $R_T(\omega, Q^2)$ are the Longitudinal and Transverse Response Functions, respectively. R_L and R_T are independent and describe the electromagnetic response of the nucleus. R_L is related to the charge and the longitudinal component of the nuclear current, while R_T is related to the incoherent sum of contributions from the two components of the nuclear current orthogonal to the direction of the virtual photon. To separate the two responses, at least two measurements in different electron kinematical settings must be made, keeping $\mathbf{q}$ and ω fixed. This type of experiment is called a Rosenbluth separation [12].

1.2.2 Semi-Exclusive Electron Scattering

An inclusive cross section contains many exclusive reaction channels. To study and evaluate the effects of these different channels on the inclusive cross section, semi-exclusive $(e, e'p)$ experiments are performed. In semi-exclusive experiments, the contributions from different valence states and the continuum channels can be discerned. Further, the longitudinal and transverse responses of these different channels may be studied.

[5] These modes are often referred to as the Giant-Dipole and Giant-Quadrupole Resonances.
[6] Δ and N^* Resonances are excited states of a nucleon.

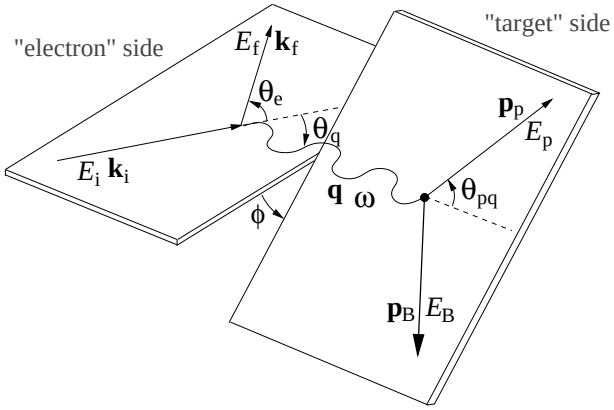

Figure 1.3: The Feynman diagram for $(e, e'p)$ in the Born Approximation.

The $(e, e'p)$ reaction in the Born Approximation is illustrated in Figure 1.3. The figure can be divided into two parts — the "electron" side and the "target" side. On the electron side, the scattering plane is defined by the initial electron momentum $\mathbf{k}_\mathrm{i}$ and the scattered electron momentum $\mathbf{k}_\mathrm{f}$. The magnitude q and direction θ_q of the transferred momentum $\mathbf{q}$ is completely determined by $\mathbf{k}_\mathrm{i}$ and $\mathbf{k}_\mathrm{f}$.

On the target side, the reaction plane is defined by the momentum of the recoil nucleus $\mathbf{p}_\mathrm{B}$ and that of the ejected proton $\mathbf{p}_\mathrm{p}$. Two important quantities not illustrated are the missing momentum $\mathbf{p}_\mathrm{miss}$ and the missing energy E_miss

$$\mathbf{p}_\mathrm{miss} \equiv \mathbf{p}_\mathrm{p} - \mathbf{q}, \tag{1.7}$$

$$E_\mathrm{miss} \equiv \omega - T_\mathrm{p} - T_\mathrm{B}, \tag{1.8}$$

where T_p and T_B are the kinetic energies of the ejected proton and the recoil nucleus, respectively. The angle between the reaction plane and the scattering plane is defined as the out-of-plane angle ϕ. If the proton is detected at $\phi = 0°$ or $\phi = 180°$, the scattering plane and the reaction plane coincide and the measurement is said to be performed "in-plane". The angle between $\mathbf{p}_\mathrm{p}$ and $\mathbf{q}$ is denoted by θ_pq. Measurements along $\mathbf{q}$ ($\theta_\mathrm{pq} = 0°$) correspond to "parallel" kinematics, as $\mathbf{p}_\mathrm{miss}$ is parallel (or anti-parallel) to $\mathbf{q}$. Measurements at all other values of θ_pq are said to be made in "quasi-perpendicular" kinematics.

As in this experiment, if neither the beam nor the target are polarised, the six-fold differential coincidence $(e, e'p)$ cross section can be expressed in terms of four independent response functions

$$\frac{d^6\sigma}{d\Omega_\mathrm{e} d\omega d\Omega_\mathrm{p} dE_\mathrm{p}} = K\sigma_\mathrm{M}\left(v_\mathrm{L}R_\mathrm{L} + v_\mathrm{T}R_\mathrm{T} + v_\mathrm{LT}R_\mathrm{LT}\cos\phi + v_\mathrm{TT}R_\mathrm{TT}\cos 2\phi\right), \tag{1.9}$$

where

$$K \equiv \frac{p_\mathrm{p}E_\mathrm{p}}{(2\pi)^3}, \tag{1.10}$$

$$v_{\rm L} \equiv \frac{Q^4}{\mathbf{q}^4}, \tag{1.11}$$

$$v_{\rm T} \equiv \frac{Q^2}{2\mathbf{q}^2} + \tan^2(\theta_{\rm e}/2), \tag{1.12}$$

$$v_{\rm LT} \equiv \frac{Q^2}{\mathbf{q}^2}\left[\frac{Q^2}{\mathbf{q}^2} + \tan^2(\theta_{\rm e}/2)\right]^{\frac{1}{2}}, \tag{1.13}$$

$$v_{\rm TT} \equiv \frac{Q^2}{2\mathbf{q}^2}. \tag{1.14}$$

The four response functions $R_{\rm L}$, $R_{\rm T}$, $R_{\rm LT}$ and $R_{\rm TT}$ depend upon $\mathbf{q}$, ω, $\mathbf{p}_{\rm miss}$ and $E_{\rm miss}$, and contain all the information that can be extracted using the $(e, e'p)$ reaction. They are related to the nuclear charge density (ρ) and nuclear current density (J) according to

$$R_{\rm L} = \langle \rho \rho^\dagger \rangle \tag{1.15}$$

$$R_{\rm T} = \langle J_\parallel J_\parallel^\dagger + J_\perp J_\perp^\dagger \rangle \tag{1.16}$$

$$R_{\rm LT}\cos(\phi) = -\langle \rho J_\parallel^\dagger + J_\parallel \rho^\dagger \rangle \tag{1.17}$$

$$R_{\rm TT}\cos(2\phi) = \langle J_\parallel J_\parallel^\dagger - J_\perp J_\perp^\dagger \rangle. \tag{1.18}$$

$J_\parallel$ and $J_\perp$ are components of the current density orthogonal to the transferred momentum $\mathbf{q}$, with $J_\parallel$ parallel to and $J_\perp$ perpendicular to the scattering plane.

Here, $R_{\rm LT}$ is the response resulting from interference between the longitudinal and transverse components, and $R_{\rm TT}$ is the response coming from interference between the two transverse components. In a parallel kinematics measurement, the finite detector aperture effectively integrates over the azimuthal angle ϕ, such that $R_{\rm LT}$ and $R_{\rm TT}$ may not be extracted.

By measuring the $(e, e'p)$ cross section for a range of values of $\mathbf{p}_{\rm miss}$ and $E_{\rm miss}$, it is in principle possible to determine the distribution of momenta and energies of the protons inside the nucleus.

Finally, one last important parameter is the longitudinal-transverse asymmetry $A_{\rm LT}$

$$A_{\rm LT} = \frac{d^6\sigma_- - d^6\sigma_+}{d^6\sigma_- + d^6\sigma_+}, \tag{1.19}$$

where $d^6\sigma_-$ is the six-fold differential cross section for $\phi = 0^\circ$ and $d^6\sigma_+$ is the cross section for $\phi = 180^\circ$; that is, for the same proton scattering angle on either side of $\mathbf{q}$[7]. $A_{\rm LT}$ is particularly valuable when comparing the results of an experiment with predictions from different theoretical models as it is systematically very precise. This is because all of the systematic uncertainties associated with measuring the scattered electron divide out in the quotient leaving only those associated with measuring the knocked-out proton. $A_{\rm LT}$ is hence much easier to extract than a response function.

[7]These correspond to negative and positive values of $\mathbf{p}_{\rm miss}$, respectively. See Section 1.3 for the definition of $\mathbf{p}_{\rm miss}$.

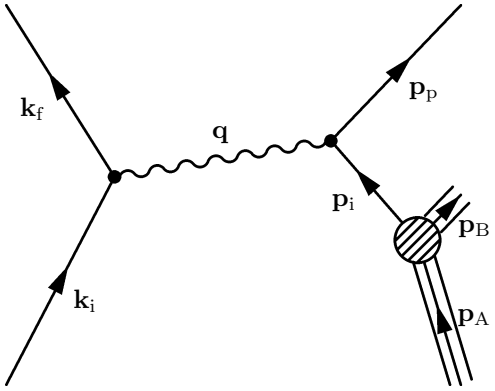

Figure 1.4: The Feynman diagram for the Plane-Wave Impulse Approximation in $(e, e'p)$. The ejected proton $\mathbf{p}_\mathrm{p}$ and the recoil nucleus $\mathbf{p}_\mathrm{B}$ do not interact subsequent to the scattering event.

1.3 The Impulse Approximation (IA)

1.3.1 Plane-Wave IA (PWIA)

In the Plane-Wave Impulse Approximation (PWIA), three assumptions are made.

1. The virtual photon is completely absorbed by a single proton in the target, and that proton receives all of the transferred energy and momentum;

2. the struck proton is ejected without any further interaction with the recoil nucleus, and it can be represented by a plane wave;

3. the target nucleus can be described by an Independent-Particle Model (IPM).

Using these assumptions, the $(e, e'p)$ cross section can be factorised as

$$\frac{d^6\sigma}{d\Omega_\mathrm{e} d\omega d\Omega_\mathrm{p} dE_\mathrm{p}} = K'\sigma_\mathrm{ep} S(E_\mathrm{miss}, \mathbf{p}_\mathrm{miss}), \tag{1.20}$$

where K' is a kinematical factor and σ_ep is the probability for scattering an electron from a proton when the proton is bound in the initial state and unbound in the final state. $S(E_\mathrm{miss}, \mathbf{p}_\mathrm{miss})$ is the Spectral Function, which can be interpreted as the probability of finding a proton with initial momentum $\mathbf{p}_\mathrm{miss}$ and binding energy E_miss inside the nucleus. Hence, in this simple model, $\mathbf{p}_\mathrm{miss}$ can be interpreted as the initial proton momentum $\mathbf{p}_\mathrm{i}$ inside the nucleus, and E_miss as the binding energy of the proton.

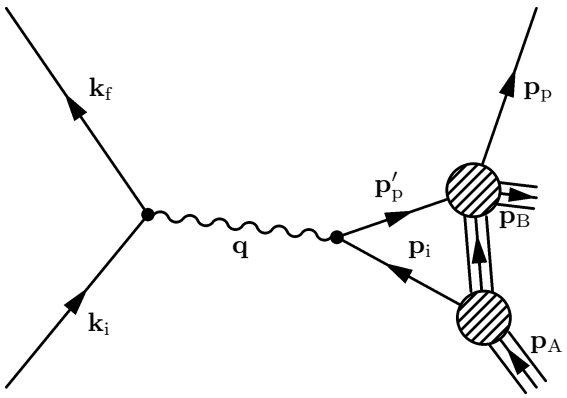

Figure 1.5: The Feynman diagram for the Distorted-Wave Impulse Approximation in $(e, e'p)$.

1.3.2 Distorted-Wave IA (DWIA)

In the PWIA, the weakest assumption is the second one — that there is no interaction between the ejected proton and the recoil nucleus. The Distorted-Wave Impulse Approximation (DWIA) takes FSI into account, while maintaining the other assumptions. FSI are usually addressed using a potential model (historically referred to as an Optical Potential) to derive the distorted wave for the ejected proton. The optical potential represents the effect of the $(A-1)$ nucleons on the knocked-out proton as it is trying to leave the target. Under these assumptions, the cross section factorises as

$$\frac{d^6\sigma}{d\Omega_\mathrm{e} d\omega d\Omega_\mathrm{p} dE_\mathrm{p}} = K'\sigma_\mathrm{ep} S^\mathrm{D}(E_\mathrm{miss}, \mathbf{p}_\mathrm{miss}, \mathbf{p}_\mathrm{p}), \tag{1.21}$$

where $S^\mathrm{D}(E_\mathrm{miss}, \mathbf{p}_\mathrm{miss}, \mathbf{p}_\mathrm{p})$ is the Distorted Spectral Function. The interpretations made for $\mathbf{p}_\mathrm{miss}$ and E_miss in the PWIA are no longer valid. DWIA is more realistic and successful in predicting experimental data. Modern Relativistic DWIA is highly successful in predicting data for $Q^2 \leq 0.8$ (GeV/c)^2 [13].

1.4 Previous Experimental Work

^{16}O$(e, e'p)$ experiments with $Q^2 < 0.4$ (GeV/c)^2 have previously been performed at Saclay (France), NIKHEF (the Netherlands) and Mainz (Germany). A summary of these experiments is presented in Table 1.1.

Figure 1.6 shows an E_miss spectrum measured at NIKHEF [14]. The spectrum is dominated by the two peaks at 12.1 MeV and 18.4 MeV, corresponding to proton knock-out from the $1p_{1/2}$ and $1p_{3/2}$ states in Figure 1.1. Due to the extremely good energy resolution at NIKHEF, the $1d_{5/2}2s_{1/2}$ doublet at 17.4 MeV as well as a pair of $3/2^-$ states at 22.0 and 22.8 MeV were also distinguishable.

Different optical potentials were also tested. Figure 1.7 shows how the resulting predictions for the momentum distributions of the p-shell agreed with the data.

Authors	Site	Kinematics	$T_{\rm p}$ (MeV)	Q^2 (GeV/c)^2
Leuschner *et al.* [14]	NIKHEF	parallel	96	varied
Spaltro *et al.* [15]	NIKHEF	perpendicular	84	0.20
Chinitz *et al.* [16]	Saclay	perpendicular	160	0.30
Bernheim *et al.* [17]	Saclay	perpendicular	100	0.19
Blomqvist1 *et al.* [18]	MAMI	parallel	92	0.08
Blomqvist2 *et al.* [18]	MAMI	highly varied	215	0.04 - 0.26

Table 1.1: Previous ^{16}O$(e,e'p)$ experimental work. NIKHEF is located in the Netherlands, Saclay in France and MAMI in Germany.

Here, the momentum distributions are plotted versus $p_{\rm miss}$ for protons in the $1p_{1/2}$ and $1p_{3/2}$ states for $-180 \leq p_{\rm miss} \leq 270$ MeV/c.

The response functions have also been extracted in these low-Q^2 kinematics, and Figure 1.8 shows a comparison of these data to a modern relativistic DWIA calculation (presented in [13]) for $30 \leq p_{\rm miss} \leq 190$ MeV/c. Clearly, agreement betwen calculations and data improves with increasing Q^2.

In the summer of 1997, the precursor to this experimental work [13, 19, 20] was performed in Hall A at JLab. The waterfall target was used, and quasielastic

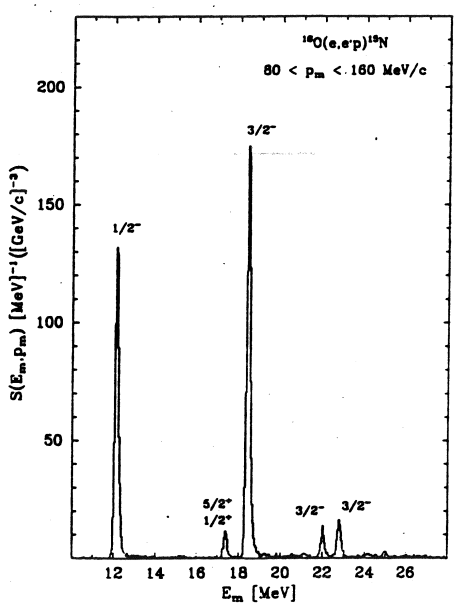

Figure 1.6: Missing-energy distribution measured at NIKHEF [14] for ^{16}O$(e,e'p)$ at $Q^2 = 0.19$ (GeV/c)^2. The $1/2^-$ state at 12.1 MeV and $3/2^-$ state at 18.4 MeV correspond to proton knock-out from the $1p_{1/2}$ and $1p_{3/2}$ states shown in Figure 1.1.

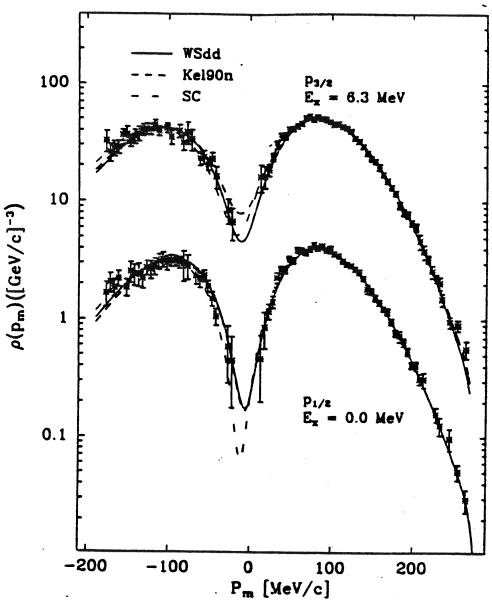

Figure 1.7: Missing-momentum distributions measured at NIKHEF [14] for $^{16}\mathrm{O}(e,e'p)$ at $Q^2 = 0.19$ (GeV/c)^2. The top and bottom data correspond to the $1p_{3/2}$ and the $1p_{1/2}$ states, respectively ($E_x = 0.0$ MeV and $E_x = 6.3$ MeV are the excitation energies in the residual ^{15}N nucleus). WSdd, Kel90n and SC were DWIA calculations with different optical potentials used to explain the data.

kinematics were employed at $Q^2 = 0.802$ (GeV/c)^2, $|\mathbf{q}| = 1.000$ GeV/c and $\omega = 445$ MeV. Data were obtained for the $1p$-shell, the $1s_{1/2}$-state and even higher energies (the continuum) for $E_{\mathrm{miss}} \leq 120$ MeV and $p_{\mathrm{miss}} \leq 375$ MeV/c. The results are presented in terms of A_{LT} in Figure 1.9.

More data were clearly needed at higher p_{miss} to allow the bound-nucleon wave function, the current operator and the optical potential to be determined independently.

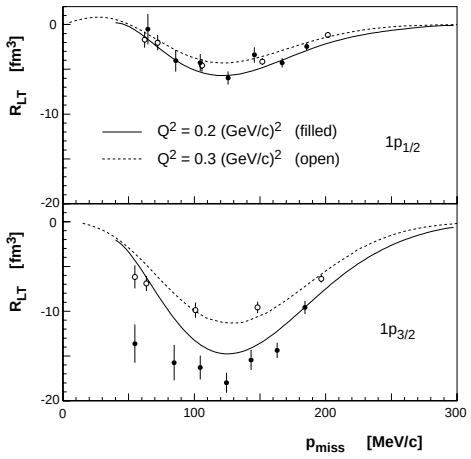

Figure 1.8: Longitudinal-transverse response functions $R_{\rm LT}$ for $^{16}{\rm O}(e,e'p)$ extracted in previous experiments. Filled circles are from NIKHEF [15] at $Q^2 = 0.20$ (GeV/c)^2 and correspond to the data shown in Figures 1.6 and 1.7. Open circles are from Saclay [16] at $Q^2 = 0.30$ (GeV/c)^2. The curves are modern Relativistic DWIA calculations (presented in [13]). The top panel corresponds to the knock-out of a proton from the $1p_{1/2}$ state, and the bottom panel from the $1p_{3/2}$ state.

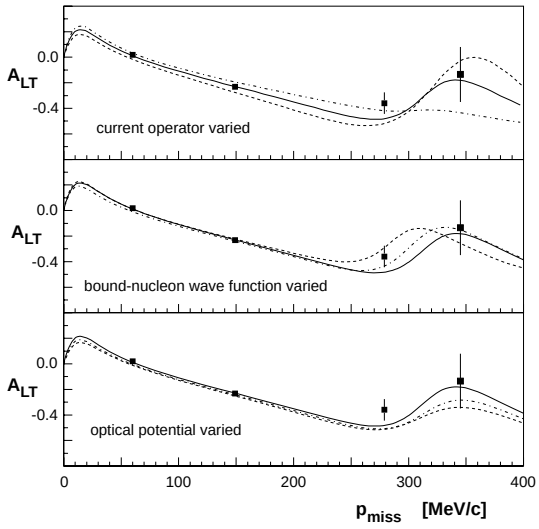

Figure 1.9: Illustration of how $A_{\rm LT}$ calculations by Udías *et al.* with different input parameters compare with the data from the E89-003 experiment. The top panel shows the effect of varying the current operator. The middle panel shows the effect of varying the bound-nucleon wave function. The bottom panel shows the effect of varying the optical potential.

Chapter 2

Experimental Method

This chapter presents an overview of the experimental equipment and method. For further information about JLab and Hall A, the interested reader is directed to [21] and the URLs `http://www.jlab.org` and `http://hallaweb.jlab.org`.

2.1 The Accelerator

The Continuous Electron Beam Accelerator Facility (CEBAF) at JLAB is presently a superconducting 6 GeV recirculating linac capable of delivering simultaneous electron beams to three experimental halls, with currents ranging from 10 nA to 120 μA. The maximum total current available to the three experiment halls is almost 200 μA CW.

CEBAF has two live electron sources used for injecting 45 MeV electrons into the accelerator; one thermionic gun and one polarised gun. There are also several guns in reserve. The polarised gun was used for this experiment, but the electron spins were systematically flipped on a sequential bunch basis so that the average polarisation was zero; that is, the beam was unpolarised.

The 45 MeV electrons which left the injector were separated into three interleaved 499 MHz bunch trains and accelerated to their ultimate energies by recirculating the beam four times through two superconducting linacs. Each linac contained 20 cryomodules producing up to 570 MeV in total per pass. One such bunch train was delivered to Hall A. As previously mentioned, this experiment used 4.620 GeV electrons at currents of up to 120 μA.

2.2 Extraction/Hall A

As shown in Figure 2.2, several instruments were necessary to guide the beam onto the target and further along onto the electron dump in a precise and reproducible fashion. It was also important to be able to simultaneously measure properties of the beam, such as its energy, current, polarisation, position and

Figure 2.1: Jefferson Lab seen from the air. The racetrack in the upper left-hand corner is the accelerating linacs and re-circulating arcs, and the three circular mounds in the bottom right-hand corner are the experimental halls. Hall A is to the left, Hall B is in the middle and Hall C is to the right. Just above Hall B is the Counting House, from where the experiments are controlled. The low building with yellow roof next to the left linac is the Machine Control Center (MCC).

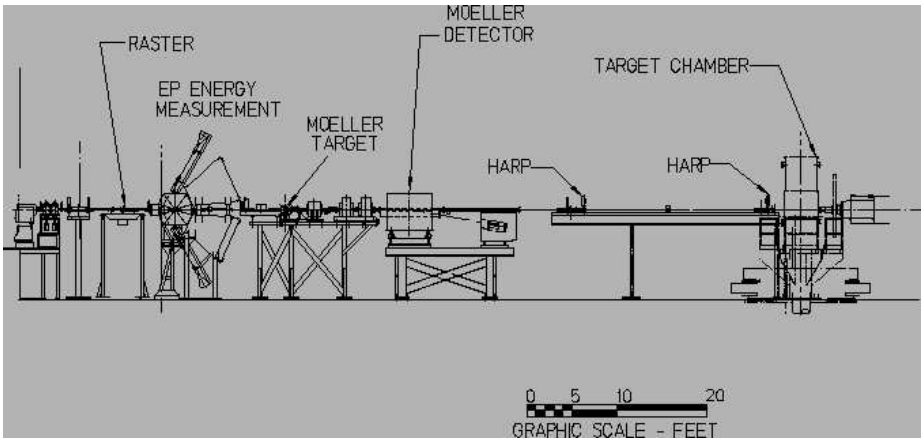

Figure 2.2: The Hall A beamline upstream of the target. The beam enters to the left and exits to the right.

direction — most often without disturbing it. Two or more independent methods were used to measure and monitor these different beam parameters in order to give confidence in the absolute measurements and to provide redundancy in the system if any of the instrumentation failed during the experiment.

Beam-diagnostic instrumentation consisted of Beam-Position Monitors (BPMs), Beam-Current Monitors (BCMs), wire scanners (HARPs), viewers and Optical Transition Radiation (OTR) viewers. The beam-optics elements used for steering the beam consisted of dipoles, focusing quadrupoles, sextupoles and correcting magnets.

2.2.1 Beam Position and Direction

Knowledge of the position of the beam on the target and the angle of incidence of the beam at the target was crucial. Located at distances 7.524 m and 1.286 m upstream of the target, two Beam-Position Monitors (BPMs) determined the position and direction of the beam at the target. Each BPM consisted of four static antennas, two for determining the laboratory horizontal position and two for the laboratory vertical position of the beam. The antenna signals were used to determine the relative position of the beam to within 100 μm. The absolute position of the beam was determined from the BPMs by calibrating them with respect to two wire scanners (HARPs) which were located in the vicinity of the BPMs and could be stepped through the beam. This cross-calibration was performed at four different occasions during the experiment to maintain confidence in the BPM readback. The wire scanners, in turn, were surveyed to give the absolute position of the beam with respect to the Hall A laboratory coordinate system.

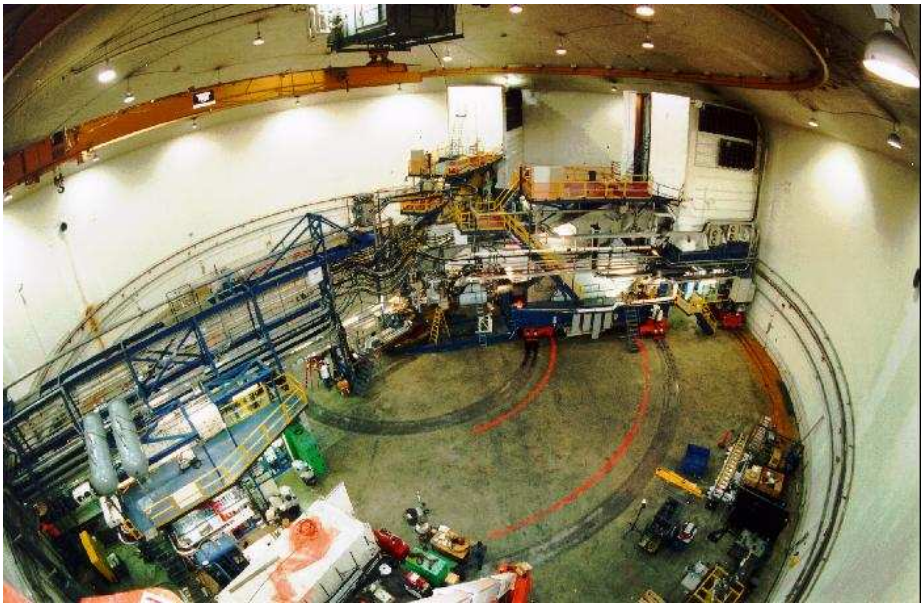

Figure 2.3: Overview of Hall A. The beamline enters the hall at lower left and the target is in the middle of the hall. The two spectrometers (shown here in a 'Y' configuration) with their 1 m thick white concrete shielding huts and yellow railings, point at the target.

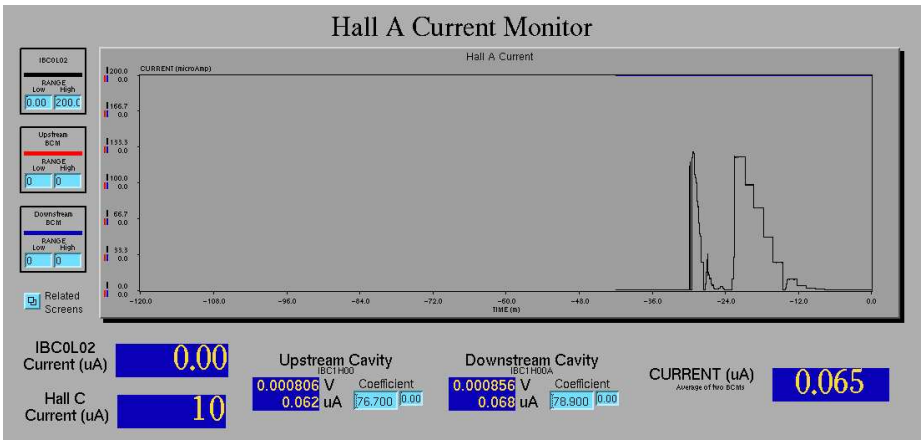

Figure 2.4: Hall A Current Monitor screen capture during BCM calibration.

The beam position information from the BPMs was recorded in two different ways:

1. The position averaged over 0.3 s was logged to a database once per second and put into the datastream every 3–5 s.

2. Event-by-event information from each of the 8 BPM antennas was put into the CODA[1] datastream.

2.2.2 Current and Charge Measurements

The Beam-Current Monitor (BCM) consisted of an Unser monitor and two RF-cavities located 25 m upstream of the target location.

Each of the output signals from the two RF-cavities was split and passed to different sets of electronics. One of the split signals was used for sampling the data at 1 Hz intervals and was recorded in the datastream of the detector Data AcQuisition (DAQ). The other signal was integrated to give the total beam charge. As the integrating electronics were not linear for all currents, that signal was in turn split into three signals, two of which were amplified by factors of 3 and 10, respectively. Each signal was recorded in scalers in both spectrometers giving a twelve-scaler redundancy for determining the total beam charge during a run.

In general, the incident beam charge for a run was determined with an accuracy of $\leq 0.5\%$ for currents as low as 0.5 μA. To calibrate the cavities, the electron beam in the accelerator was reduced from 120 μA to 20 μA in steps of 20 μA (see Figure 2.4), and measurements performed for 90 s at each intensity. The readout of the BCM was then compared with the charge measured in the Faraday Cup at the beam dump, and a calibration factor thus determined.

[1] CEBAF On-line Data Acquisition System, see Section 2.6.

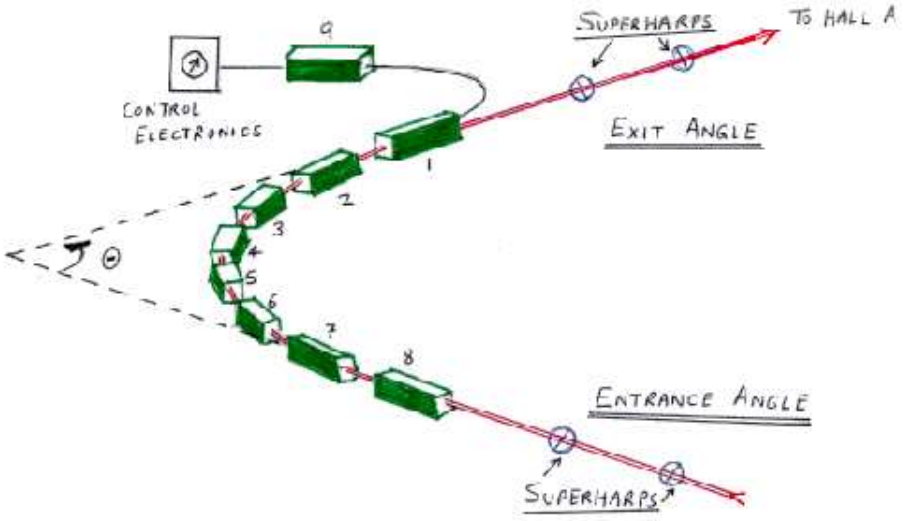

Figure 2.5: Overview of the magnets used in the ARC absolute beam-energy measurement. The beam enters at bottom right and exits at top right. Eight arc dipoles are shown in a chain. The ninth reference dipole is also shown together with the control electronics.

2.2.3 Absolute Energy Measurements

The absolute energy of the electron beam was measured using two independent methods: the Arc Method and the eP Method.

The Arc Method was used to determine the energy by measuring the deflection of the electron beam in the arc section of the beamline between the extraction point at the accelerator and Hall A. The nominal bend angle of the beam in the arc section was 34.3°. The momentum of the beam (p in GeV/c) was then related to the field integral of the eight dipoles ($\int \mathbf{B} \cdot \mathbf{dl}$ in Tm) and the bend angle through the arc section (θ in radians) by

$$p = c \cdot \frac{\int \mathbf{B} \cdot \mathbf{dl}}{\theta}, \tag{2.1}$$

where $c = 0.299792458$ GeV·rad/Tm. The magnetic-field integral of the bending elements (the eight dipoles in the arc) was determined using a reference magnet (a 9th identical dipole stationed permanently in the Test Lab), and the measurement of the actual bend angle of the arc was determined using a set of wire scanners.

The eP device was located 17 m upstream of the target. Here, the beam energy was determined via a coincidence elastic ^{1}H(e, ep) measurement. The scattered electron angle θ_e and the recoil proton angle θ_p were used to determine the beam energy according to

$$E = M_p \frac{\cos(\theta_e) + \sin(\theta_e)/\tan(\theta_p) - 1}{1 - \cos(\theta_p)} + \mathcal{O}(m_e^2/E^2). \tag{2.2}$$

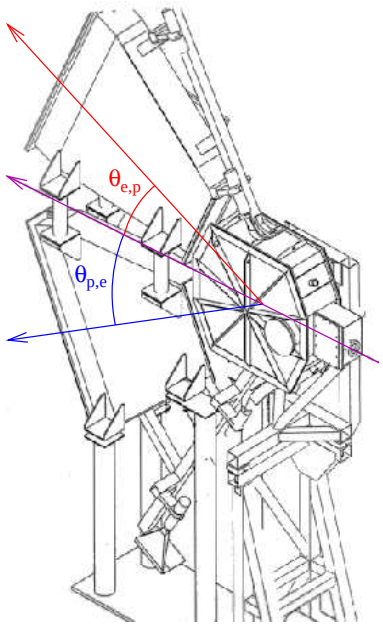

Figure 2.6: Overview of the eP detectors used for absolute beam-energy measurements. A thin CH_2 wafer providing proton targets was inserted into the beam at the centre of the device. The electrons in the beam (purple) collide with the protons in a two-body interaction. The scattered electrons (red or blue) and the recoil protons (blue or red) were detected in a coincidence measurement in the two detector arms.

Here, M_p was the mass of the proton and $\mathcal{O}(m_\mathrm{e}^2/E^2)$ was small. The hydrogen target was a thin CH_2 wafer inserted into the beamline. Two identical detector arms were placed symmetrically about the beam within the laboratory vertical plane and a coincidence measurement between the scattered electron and recoil proton performed.

Method	Date	Energy (MeV)
Arc	Oct 29	4618.6
Arc	Nov 2	4617.5
eP	Nov 11	4619.1
eP	Dec 7	4618.3

Table 2.1: Results from ARC and eP measurements giving a mean value for the electron beam energy over the entire run period of 4618.4 MeV. Uncertainties are smaller than 1.4 MeV.

Repeated measurements of the beam energy using both methods gave a mean value for the electron beam energy of 4618.4 MeV (Table 2.1) and demonstrated self-agreement to within $\leq 3 \cdot 10^{-4}$ over the course of the entire experiment.

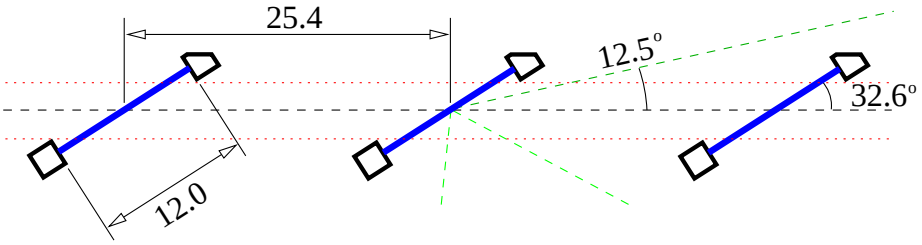

Figure 2.7: The layout of the waterfall target from above. The beam entered from the left and exited to the right. Electrons were detected at 12.5° beam left (above in the picture) and protons at various angles between 28° and 96° beam right (between the green dashed lines; below in the picture). Dimensions are given in mm.

2.3 The Target System

The standard vacuum scattering chamber was constructed from several rings. The middle ring was made of aluminium and vertically centred at beam height with a rectangular window on each side of the beam. The windows spanned the full angular range ($12.5° < \theta \leq 165°$) accessible to the spectrometers. There were no vacuum couplings to the spectrometers; rather, the windows were covered with flanges with thin (0.38 mm) aluminium foils (which caused some energy loss for charged particles passing through them).

The waterfall target was placed inside the scattering chamber. In the target cell, water was forced through vertical slits to form three flat, vertical, rectangular foils. These foils were stable due to surface tension and the adherence of the water to the stainless-steel poles. The water, continuously pumped from a reservoir outside the scattering chamber, passed through a heat exchanger into the target cell, and then back into the reservoir. All parts in contact with the water were made of stainless steel.

Once the target foils were formed, the thickness of the foils increased with the pump speed up to a maximum value which depended essentially on the dimensions of the slits through which the water passed (see Figure 2.8). A tachometer measured the pump speed. A flow meter, located upstream of the entrance to the scattering chamber, measured the flow rate. The target-thickness stability was monitored continuously by measuring these parameters[2]. A cooler was used to keep the water at a constant temperature.

A configuration with three identical waterfalls was used, with each waterfall nominally 125 mg/cm^2 (0.125 cm) thick, and oriented at 32.6° to the incident beam direction (see Figure 2.7). This configuration was better than a single waterfall three times as thick because the energy loss in the target was reduced. The foil angles were optimised with respect to the apertures of the spectrometers and the trajectories of the ejected particles, so that neither the scattered

[2]Elastic electron scattering from the ^{1}H in the target allowed for the target thickness to be continuously monitored by observing the electron singles rates in the HRS$_1$. See Section 3.4.2.

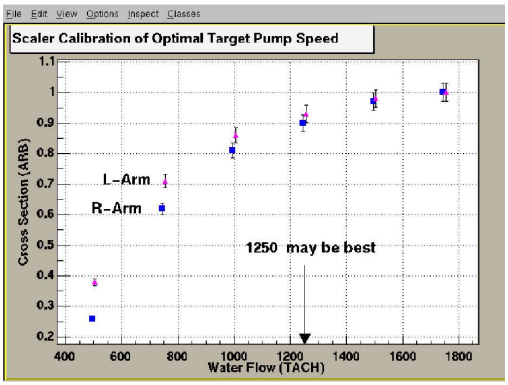

Figure 2.8: Pump-speed calibration. The target thickness was analysed by looking at electron and proton rates normalised to beam current. The trigger rates increased when the water flow increased since the water foils became thicker. The thickness reached an asymptotic value which depended upon the dimensions of the slits in the reservoir. A value of 1250 for the water flow was chosen as an optimal trade-off between maximum foil thickness and minimum pump speed.

electrons nor the knocked-out protons went through a second waterfall for any of the kinematical settings. The foils were all identical, 12 mm wide, and guided by posts which were 2 mm $\times$ 2 mm.

The dependence of the target thickness upon the waterpump speed was mapped by looking at the spectrometer singles trigger rates at different tachometer settings (see Figure 2.8). Out of concern for the lifetime of the waterpump, it was decided not to push it to its limit. The experiment pump speed tachometer setting was chosen to be 1250 to keep the waterfalls as thick as possible without risking the pump.

As the electron beam carried a large amount of power, localised vaporisation in the waterfalls was induced. This vaporisation resulted in reduced water density; that is, fewer target nuclei. In order to look for this effect, the waterpump speed was held constant and a scan with increasing beam current was performed. Small effects ($\leq 5\%$) were seen as the current was increased.

The target cell was a box $20 \times 15 \times 10$ cm^3. The entrance and exit windows were circular (30 mm in diameter) and made of 75 μm thick beryllium, so that they could withstand the high beam current without melting. The side windows, which the scattered electrons and knocked-out protons passed through, were made of 25 μm thick stainless steel.

The outer target chamber was maintained under vacuum to reduce energy loss and multiple scattering of beam electrons, scattered electrons and ejected protons. To ensure that the target cell did not move during evacuation, a "post scan" was performed. A low-intensity electron beam was purposely mis-steered horizontally inside the empty cell to see if the waterfall posts were hit. No

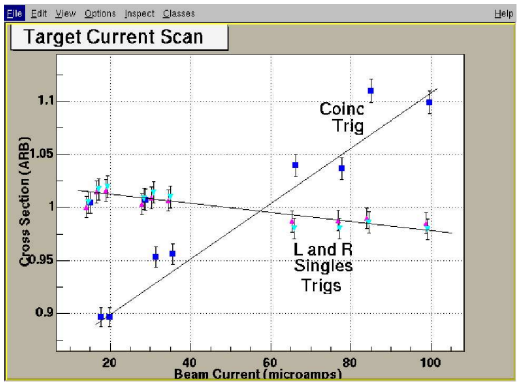

Figure 2.9: Effects on the measured "cross section" due to increasing the beam current. To remove the expected increase in trigger rates which came with increased beam current, the measured "cross section" has been divided by the beam current. It was evident that the trigger rates were stable and thus localised boiling in the water foils could be quantified. Note that the increase in the coincidence triggers was expected as random coincidences depend upon the square of the beam current.

changes in trigger rates were detected and it was thus deduced that the nominal beam trajectory was well-centered on the target. The water was then turned on and the trigger rates increased as expected, indicating that the beam indeed passed between the posts and through the water.

Beneath the cell was a target ladder which held five thin solid targets. A mechanical system driven by stepping motors allowed for a vertical movement of the target ladder in order to change the target which was placed in the beam. A density-calibrated BeO target was used to estimate the thickness of the water foils[3]. It had a thickness of 0.3692 ± 0.0002 g/cm^2.

2.4 The Spectrometers

The High Resolution Spectrometers (HRS) were designed to isolate exclusive reaction channels so that clean comparisons of data with theory can be achieved. Some general design characteristics are presented in Table 2.2.

2.4.1 Magnets

The magnetic quartet in each spectrometer was identical in layout and constituted a vertically bending optical chain (see Figure 2.10). First in the chain

[3]The number of ^{16}O nuclei per cm^2 in the BeO was known and the number of ^{16}O nuclei per cm^3 for water was known. When performing ^{16}O$(e,e'p)$ measurements on the two targets, the waterfall thickness could hence be determined by comparing the $1p_{1/2}$ yields.

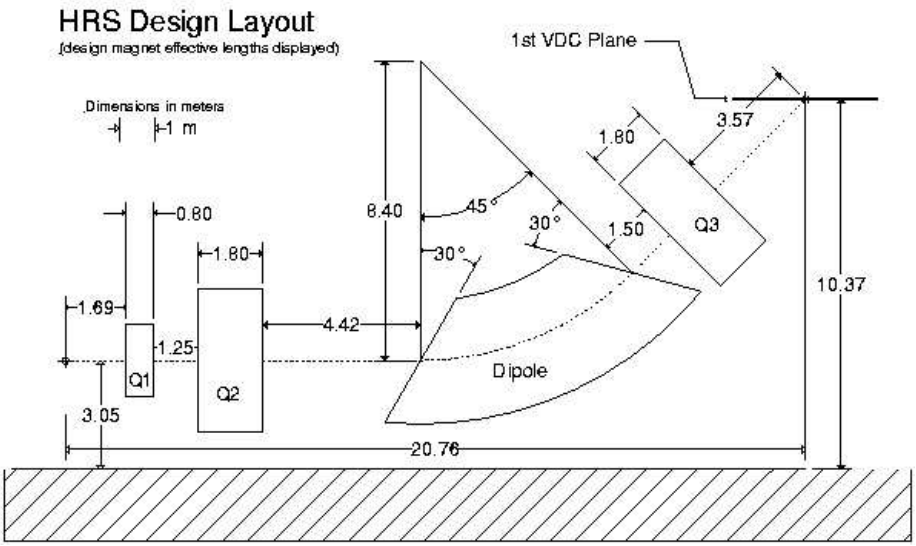

Figure 2.10: Schematic layout of the magnets in the HRS. Q1, Q2 and Q3 are quadrupoles. All are superconducting.

Configuration	QQDQ vertical bend
Bending angle	45° vertical
Optical length	23.4 m
Momentum range	0.3–4.0 GeV/c
Momentum acceptance	$-4.5\% < \delta p/p < +4.5\%$
Momentum resolution	1×10^{-4}
Solid angle at $\delta p/p = 0$, $y_0 = 0$	6 msr
Angular range	
HRS_l	12.5°–150°
HRS_r	12.5°–130°
Angular acceptance	
Horizontal	± 30 mrad
Vertical	± 60 mrad
Angular resolution	
Horizontal	0.5 mrad
Vertical	1.0 mrad

Table 2.2: Design characteristics of the HRS. The quoted resolution values are FWHM.

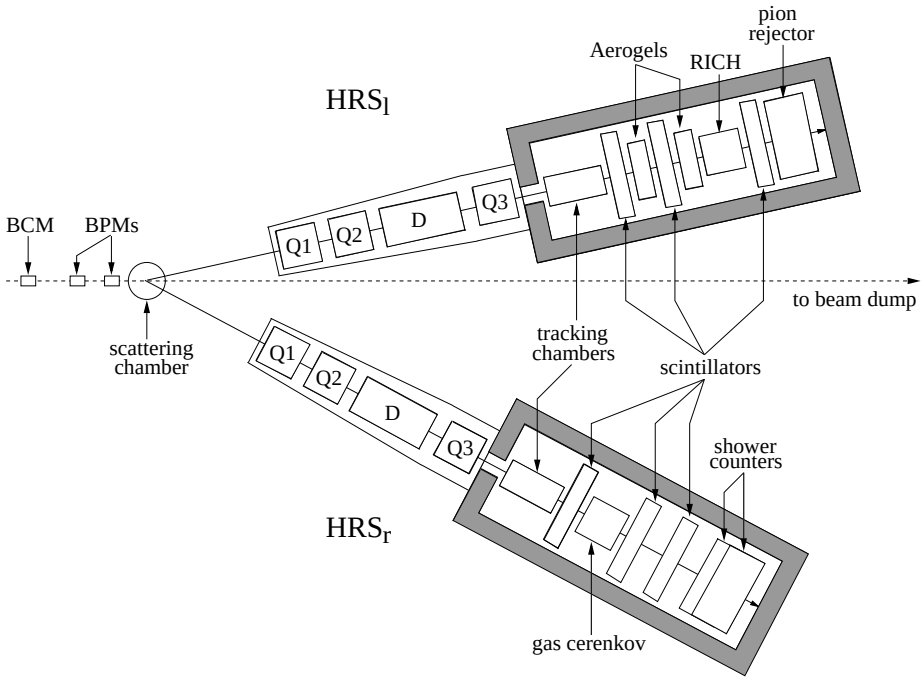

Figure 2.11: The Hall A spectrometers configured for E00-102. The electron beam passed through a Beam-Current Monitor and Beam-Position Monitors before striking a waterfall target located in the scattering chamber. Scattered electrons were detected in the HRS$_l$, while knocked-out protons were detected in the HRS$_r$. Non-interacting electrons were dumped. Note that the aerogels, the gas cerenkov and the RICH were in place but not used.

came a pair of superconducting quadrupoles (Q1 and Q2). They were followed by a 6.6 m long dipole magnet with focusing entrance and exit faces, with further focusing achieved via the use of a field gradient. The dipole magnet dispersed incoming charged particles, altering their trajectory in inverse proportion to their momentum, hence allowing for momentum measurements. Downstream of the dipole was another superconducting quadrupole (Q3). Q1 focused radially, while Q2 and Q3 focus transversally. The magnetic fields in each dipole were continually monitored using two arrays of three NMR field probes.

The position and trajectory of a particle were measured at the focal plane which was located approximately at the first VDC[4] plane. To determine the position and trajectory of a particle at the target from the focal-point coordinates, detailed knowledge of the spectrometer optics was required. Analysis of measurements made with the sieve slit collimator[5] inserted in front of the spectrometer

[4]Vertical Drift Chamber, see Section 2.5.2.

[5]The sieve slit is a 5 mm thick tungsten sheet with a pattern of 49 holes (7×7 lattice) spaced 25 mm apart vertically and 12.5 mm apart horizontally. 47 of the holes are 2 mm in diameter, while the remaining two, one in the center and one displaced 2 rows vertically and one horizontally, are 4 mm in diameter. By masking all particle trajectories save those

aperture (see Section 2.4.2) allowed for the determination of the transfer matrix.

The trajectory of a charged particle through the magnetic elements was represented by a vector whose components were the relative positions, angles and momentum of the particle with respect to a central reference trajectory

$$\vec{x} = \begin{bmatrix} x \\ \theta \\ y \\ \phi \\ l \\ \delta \end{bmatrix}, \tag{2.3}$$

where

- x was the displacement in the dispersive plane of the trajectory relative to the reference trajectory (for the HRS, $+x$ was laboratory vertical down),
- θ was the angle this trajectory made in the dispersive plane with respect to the reference trajectory ($\theta = dx/dz$, where z was the direction of the reference trajectory),
- y and ϕ were the same as x and θ but in the transverse plane (for the HRS, $+y$ was laboratory left),
- l was the path-length difference between the trajectory and the reference trajectory, and
- δ ($\Delta p/p$) was the fractional deviation of the momentum of the trajectory from the mometum of the central trajectory.

The orientation of the x, y and z-axes were such that $\hat{z} = \hat{x} \times \hat{y}$. To first order, the transfer of a charged particle from the interaction point $\vec{x}_{\rm tg}$ through the series of magnets which comprised the HRS (see Figure 2.10) to the focal point $\vec{x}_{\rm fp}$ was represented by the matrix equation

$$\begin{bmatrix} x_{\rm fp} \\ \theta_{\rm fp} \\ y_{\rm fp} \\ \phi_{\rm fp} \\ \delta_{\rm fp} \end{bmatrix} = \begin{bmatrix} -2.48 & 0.0 & 0.0 & 0.0 & 12.4 \\ -0.15 & -0.40 & 0.0 & 0.0 & 2.04 \\ 0.0 & 0.0 & -0.40 & -1.30 & 0.0 \\ 0.0 & 0.0 & 0.54 & -0.78 & 0.0 \\ 0.0 & 0.0 & 0.0 & 0.0 & 1.0 \end{bmatrix} \begin{bmatrix} x_{\rm tg} \\ \theta_{\rm tg} \\ y_{\rm tg} \\ \phi_{\rm tg} \\ \delta_{\rm tg} \end{bmatrix}. \tag{2.4}$$

2.4.2 Collimators

Each spectrometer had three collimators positioned in its "snout". There were two tapered, rectangular collimators, each made of 80 mm thick tungsten placed in a collimator stack, 1.109 m ($\rm HRS_l$) and 1.100 m ($\rm HRS_r$) downstream from the target, upstream of Q1. They were used for reducing the spectrometer acceptance. The third collimator was the sieve slit, which was used to study the optical properties of the spectrometers. The sieve slits were located 1.1755 m and 1.1843 m downstream from the target in the right and left arms, respectively.

passing through the holes, the transfer matrix describing the passage of the particles through the spectrometer magnets could be mapped.

2.5 The Detector Package

In addition to providing an event trigger to activate the DAQ electronics, the detector packages were used to determine the following properties of charged particles which passed through the spectrometer:

- position and direction (tracking information),
- precise timing (for Time-Of-Flight (TOF) measurements and coincidence determination), and
- Particle IDentification (PID).

Triggering and timing information came primarily from the scintillator planes; the main trigger was S1 AND S2. Tracking was accomplished through the use of a pair of Vertical Drift Chambers (VDCs). PID was performed with lead-glass shower counters. The detectors and all the DAQ electronics were located inside the shielding huts (see Figure 2.11) on the spectrometer platforms about 25 m from the target and about 20 m above the floor of the experimental hall.

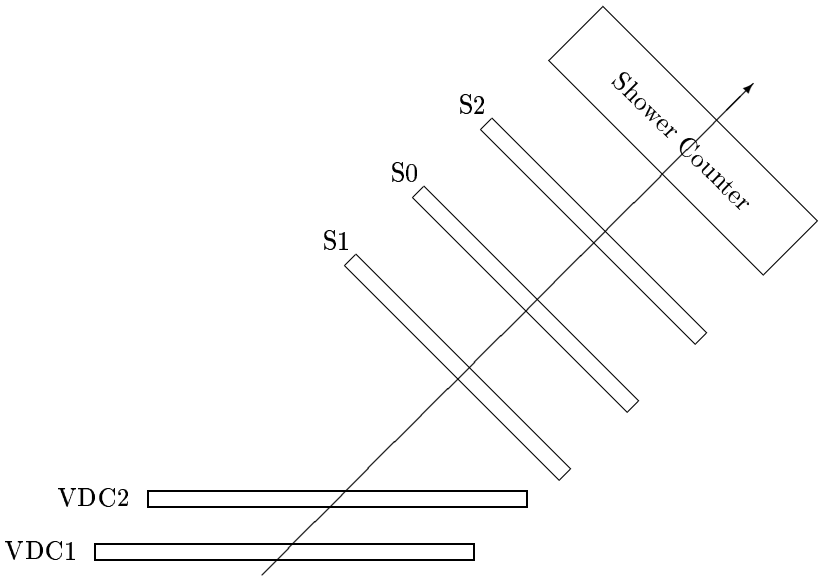

Figure 2.12: Schematic of the detector packages used in both spectrometers during this experiment. The detectors were located in the Shielding Huts, along with all the detector electronics. They were controlled remotely from the Counting House. VDC1 and VDC2 were Vertical Drift Chambers. S0, S1 and S2 were plastic scintillator trigger planes. The Shower Counter was composed of blocks of lead-glass scintillator. These detectors are described in Section 2.5.

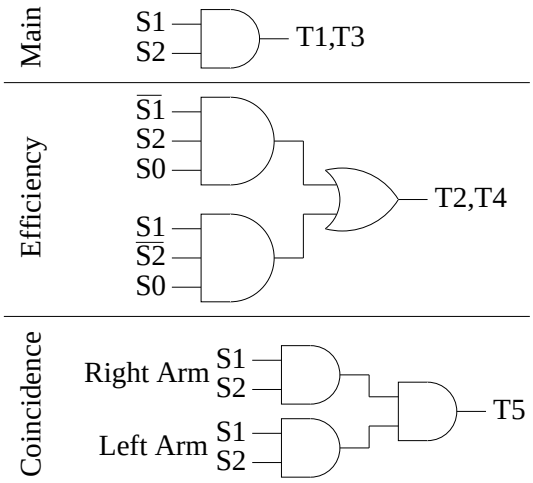

Figure 2.13: Simple overview of the trigger logic. S1 and S2 indicated the existence of a signal from one of the six paddles in scintillator planes S1 and S2, respectively. $\overline{S1}$ and $\overline{S2}$ indicated the absence of a signal from any of the paddles in S1 and S2, respectively. S0 indicated the existence of a signal from the S0 scintillator paddle. The top panel shows the main trigger logic, the middle panel shows the efficiency trigger logic and the bottom panel shows the coincidence trigger logic. For the main and efficiency triggers, if the signal originated in the HRS_r it was designated as T1 or T2, and if the signal originated in the HRS_l it was designated as T3 or T4. The coincidence trigger was designated T5.

2.5.1 Triggering and Timing

The two primary trigger scintillator planes S1 and S2 were separated by approximately 2 m. Each plane was composed of six overlapping paddles made of thin (5 mm) plastic scintillators. Each scintillator paddle was viewed by two photomultiplier tubes (PMTs). The intrinsic time resolution per plane was about 0.30 ns. An additional scintillator trigger (S0), viewed by two PMTs, was mounted between S1 and S2 to allow for a two-out-of-three trigger efficiency test based pairwise on S0, S1 and S2.

The main trigger was formed by the logical AND of the first and second scintillator planes (see Figure 2.13). To measure trigger efficiency, an alternative trigger was formed by a simultaneous hit in either the first or the second scintillator plane and a hit in the S0 scintillator. A coincidence trigger was made from the time overlap of the two spectrometer triggers in a logical AND unit. The various trigger signals were passed to a Trigger Supervisor (TS) which started the DAQ readout. Most inputs of the trigger supervisor could be individually prescaled so that only a certain fraction of less interesting triggers were accepted to reduce DAQ CPU deadtime. Typically, a 2 kHz trigger rate was used, which corresponded to a 20% CPU dead time.

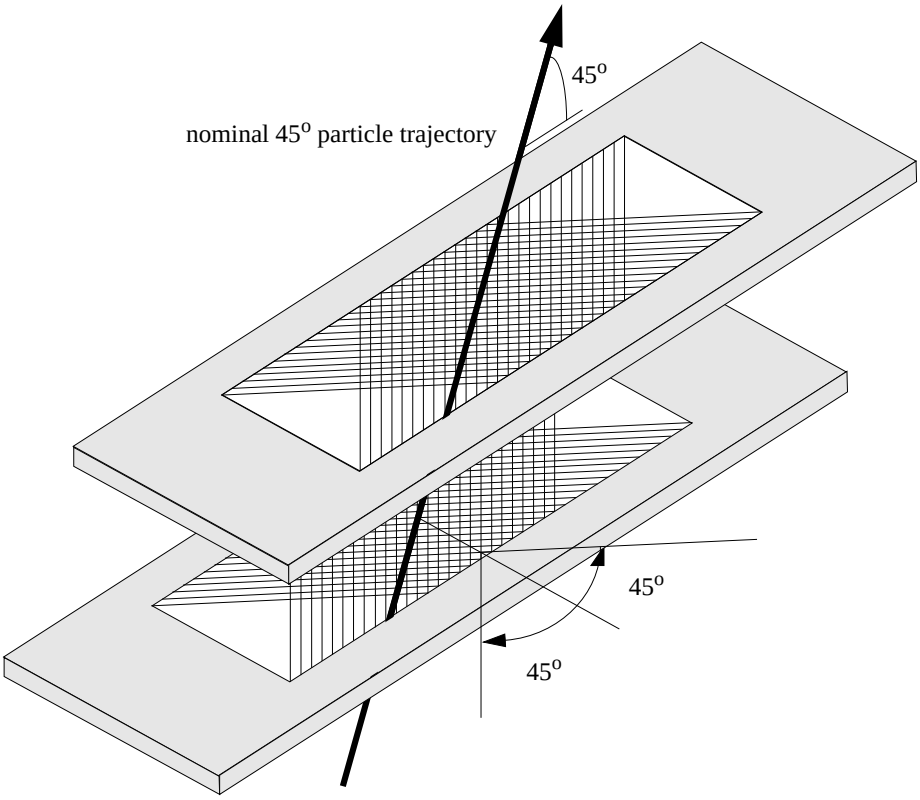

Figure 2.14: An oblique overview of the Vertical Drift Chambers (VDCs) used for tracking charged particles as they pass through the HRS. Particles entered the VDC from below at an angle of about 45° in the laboratory and left a trail of ionisation. The measured ionisation drift times to the sense wires were used to reconstruct the trajectory of the ionising particle.

2.5.2 Tracking

Tracking information was provided by a VDC pair [22] located in each spectrometer. Each VDC was composed of two sense-wire planes in a standard UV configuration – the wires of each plane were oriented 90° to one another, and each plane was oriented at 45° with respect to the dispersive direction (see Figure 2.14). There were a total of 368 sense wires in each plane. Each wire plane was sandwiched between two high voltage planes.

The VDC was filled with a gas mixture of argon (62%) and ethane (38%). When a charged particle passed through a VDC, the atoms of the gas were ionised along its path. The freed electrons drifted along the electric-field lines towards the nearest sense wire (Figure 2.15). Close to the wire, the acceleration of the electrons due to the strong electric field made it possible for them to gain enough energy to cause further ionisation. These electrons could in turn cause

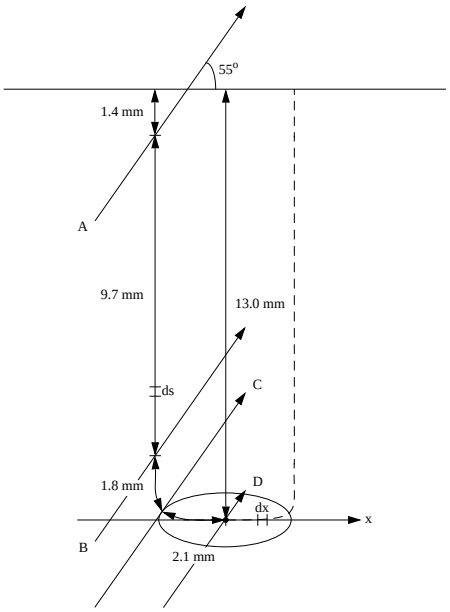

Figure 2.15: An illustration of the electric field around a sense wire. Scattered particles entered the VDC at a lab angle of about 45° from below (55° in the wire-plane coordinate system) and caused ionisation in the chamber gas along their path. Far away from the sense wire, the electric field was homogeneous and the ionised electrons travelled towards the wire. Due to collisions with the molecules in the gas, the drift velocity of the ionised electrons was constant. Very near the sense wire, the electric field grew strong and the electrons underwent an acceleration towards the wire causing avalanches along their paths.

more ionisations, creating avalanches. A TDC was used to measure the time elapsed between the initial ionisation and the induction of a signal on one or more of the sense wires. Knowledge of the electron drift velocity in the chamber gas then allowed the drift distance to be deduced (see Figure 2.16).

Generally, five or six adjacent wires gave signals from a single particle. From the drift times to the different wires, the intersection point between the trajectory and the wire plane was determined. Each wire plane gave the position along only one coordinate axis. As there were four wire planes in each spectrometer, four intersection points were thus obtained, making knowledge of the ionisation drift velocity redundant, and leading to one position coordinate $(x_{\rm fp}, y_{\rm fp})$ and two angular coordinates $(\theta_{\rm fp}, \phi_{\rm fp})$ at the focal plane. Here, the position resolution was $\sim$100 μm, and the angular resolution was $\sim$0.5 mrad.

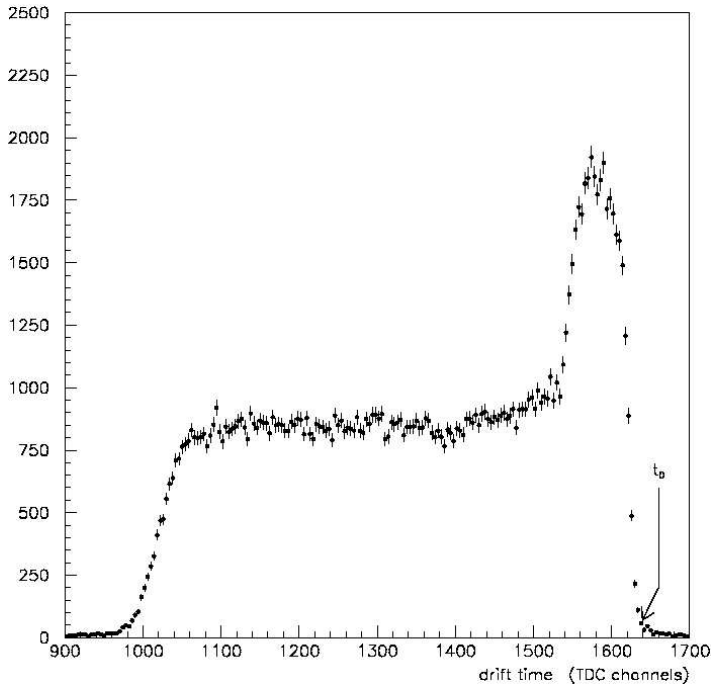

Figure 2.16: An illustration of the VDC drift-time spectrum from one sense wire. Near the sense wire, the field was strong and the drift time was short. Ionisation near the wire was quickly collected. Further away the field was weaker but constant. The resulting drift velocities of the ionised electrons were constant due to collisions with the molecules in the gas, resulting in the flat distribution. The end point of the drift spectrum is called t_0. The TDC spectra for all the sense wires were aligned to a common t_0 to facilitate the comparison of spectra from different wires.

2.5.3 Particle Identification

Time of flight (TOF) between the S1 and S2 trigger planes was used to measure the speed of the particles passing through them. The information from these detectors was used to separate protons from positive pions (see Figure 2.17).

Two layers of scintillating lead-glass shower detectors were installed in each HRS. The energy deposited in the detectors depended on the mass of the incident particle. While pions produce hardly any shower, electrons do, and the information from these detectors was thus used to separate electrons from negative pions.

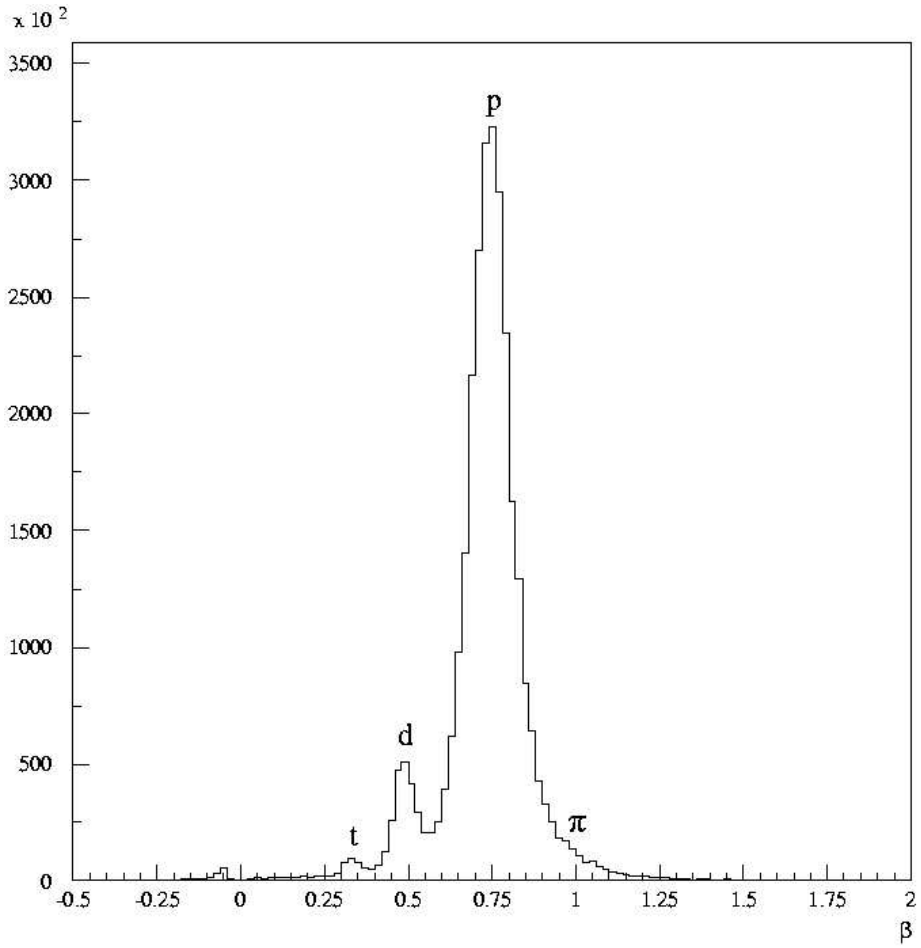

Figure 2.17: Illustration of the $\mathrm{HRS_r}$ β spectrum for PID. Peaks could be seen for tritons (t), deuterons (d) and protons (p). The hadron spectrometer had a nominal momentum setting of 1.066 GeV/c selecting protons with $\beta = 0.751$. Pions (π) with positive charge and a momentum of 1.066 GeV/c would have $\beta = 0.991$. There was no prominent feature at this value, however, and contamination from pions was thus negligible.

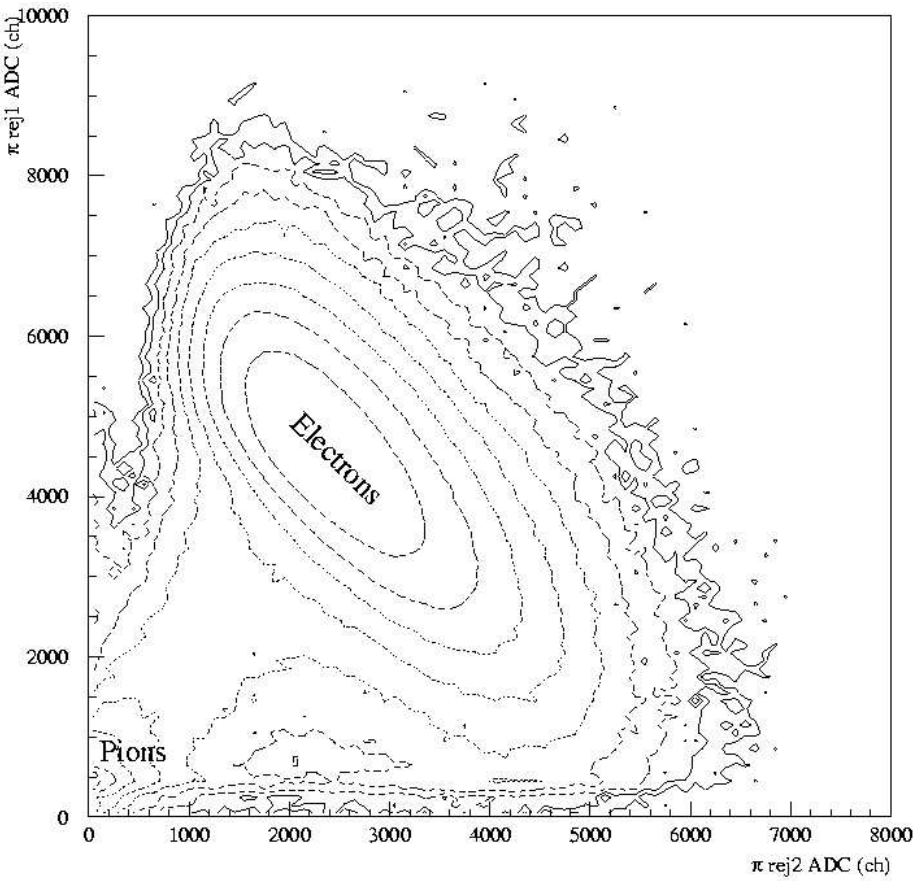

Figure 2.18: Illustration of the energy deposited in the lead-glass pion rejectors in the HRS_l. Both axes are in units of ADC channels. The energy deposited by particles in the first layer of the pion rejector is plotted on the x-axis, and the energy deposited in the second layer is plotted on the y-axis. Electrons left some of their energy in the pion rejector which resulted in the distribution dominating the plot while negative pions deposited very little energy and ended up in the distribution in the lower left corner of the plot.

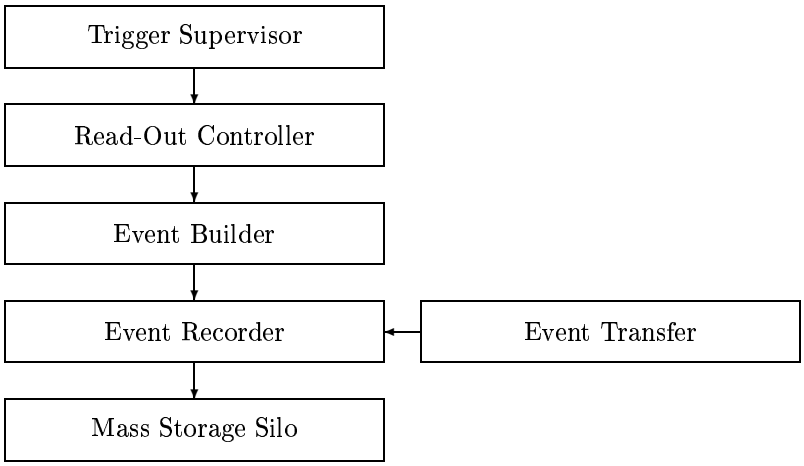

Figure 2.19: Flowchart for the Data-Acquisition (DAQ) system

2.6 Data Acquisition

The DAQ in Hall A was based upon CODA (CEBAF On-line Data Acquisition System) [21] developed by the Jefferson Lab Data-Acquisition Group. The most important custom software components of CODA were the Read-Out Controller (ROC) which ran on the front-end electronics crates, the Event-Builder (EB) and Event Recorder (ER) which ran on a Linux workstation and the Event Transfer (ET) system which allowed distributed access to the data online or insertion of data into the data stream from user processes. RunControl, finally, was a graphical user interface (GUI) from which users could select different trigger and target configurations, start and stop runs, or reset, transition and monitor CODA components.

For each event which corresponded to a trigger accepted by the Trigger Supervisor (TS), data were gathered by the ROC, buffered in memory and sent via the network to the EB. The EB assembled the events from the fragments sent by the ROCs and passed them to the ER which wrote them to a local disk. The data were eventually written to tapes in the Mass Storage Silo (MSS) and erased from the local disk after typically 24 hours. Using the ET system, some additional pieces of information from such sources as the control system, scalers and text files were inserted into the data stream every few seconds. In addition, the ET system was used by analysis clients to obtain a random sample of data in real-time anywhere on the network.

2.7 The E00-102 Experiment

The goals of this experiment [23] were to measure the $^{16}\mathrm{O}(e,e'p)$ cross section in quasielastic kinematics with higher statistical precision and to much higher missing momentum and missing energy than in E89-003. Data were taken at

Measurement	p_{miss} (MeV/c)	θ_{pq} (deg)	θ_{p} (deg)
I−	−515	−27.95	28.27
H−	−430	−23.27	32.95
G−	−345	−18.60	37.62
F−	−280	−14.90	41.32
E−	−210	−11.20	45.02
D−	−175	−9.40	46.82
C−	−140	−7.50	48.72
B−	−105	−5.60	50.62
A−	−70	−3.75	52.47
q	0	0	56.22
A+	+70	+3.75	59.97
B+	+105	+5.60	61.82
C+	+140	+7.50	63.72
D+	+175	+9.40	65.62
E+	+210	+11.20	67.42
F+	+280	+14.90	71.12
G+	+345	+18.60	74.82
H+	+430	+23.27	79.49
I+	+515	+27.95	84.17
J+	+635	+34.87	91.09
K+	+725	+39.88	96.19

Table 2.3: Overview of the kinematical settings. Settings with negative p_{miss} are said to be at "minus" kinematics and those with positive p_{miss} are said to be at "plus" kinematics. See also Figure 2.20.

$p_{\mathrm{miss}} < 300$ MeV/c to statistically improve upon and compare with the existing data. More importantly, data were also taken at $p_{\mathrm{miss}} > 300$ MeV/c where no measurements had ever before been made.

For this experiment, a beam energy of 4.620 GeV was used. The $\mathrm{HRS_l}$, set to detect electrons with a central momentum of 4.121 GeV/c, was fixed at 12.50° and was never moved. This determined the kinematical variables $|\mathbf{q}| = 1.073$ GeV/c and $\omega = 0.499$ GeV, and hence $Q^2 = 0.902$ (GeV/c)^2. The $\mathrm{HRS_r}$, detecting protons, was positioned at a number of angles given in Table 2.3, with a constant momentum setting of 1.066 GeV/c. The experimental kinematics are summarised in Table 2.3.

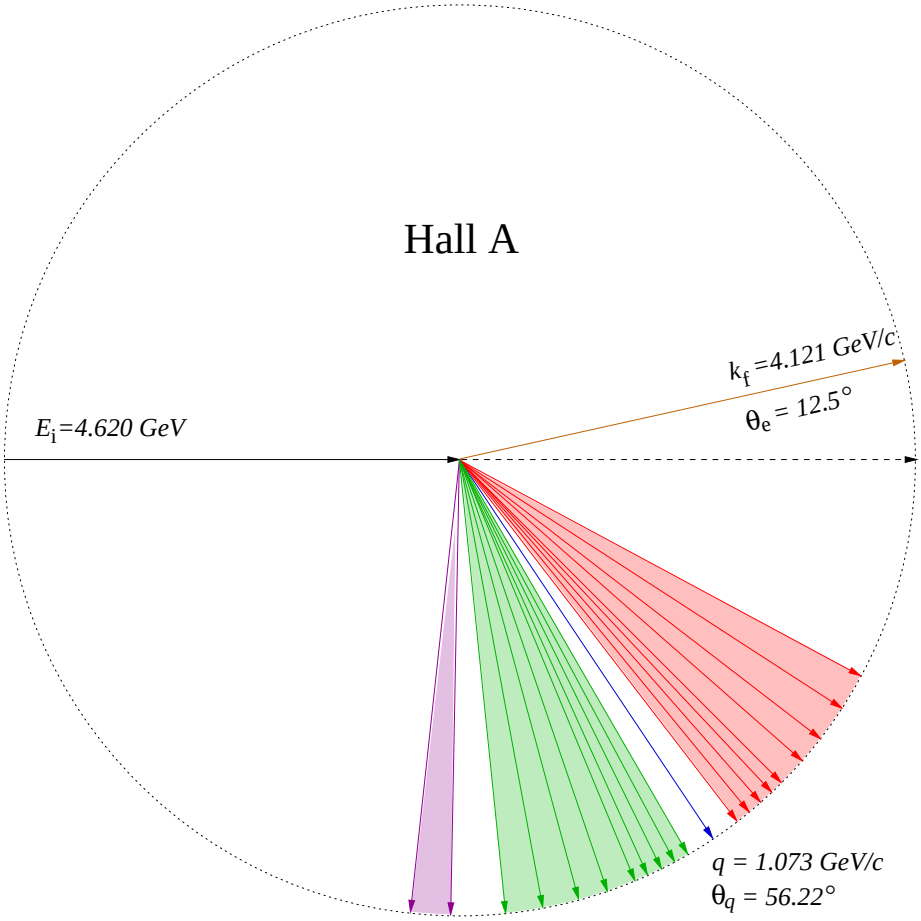

Figure 2.20: The range of kinematical settings. The 4.620 GeV electron beam entered Hall A from the left. The waterfall target was located inside the scattering chamber at the centre of the Hall. The electron spectrometer was set at $\theta_e = 12.5°$ (brown) with a central field of 4.121 GeV/c, thus determining the magnitude and direction of the momentum transfer (blue) to be 1.073 GeV/c at $\theta_{pq} = 56.22°$. Measurements of ejected protons were made at a range of angles and thus p_{miss} (see Table 2.3). Red indicates "minus" kinematics (negative p_{miss}) and green indicates "plus" kinematics (positive p_{miss}). Magenta corresponds to groundbreaking measurents performed at extreme positive p_{miss}.

Chapter 3

Analysis

In this chapter, the offline data analysis performed to date is presented. The aim of this thesis was to extract the relative cross section for kinematics A+ to F+ (70 MeV/c < p_{miss} < 280 MeV/c). The procedure to reach that aim and the problems encountered along the way are described.

3.1 Overview

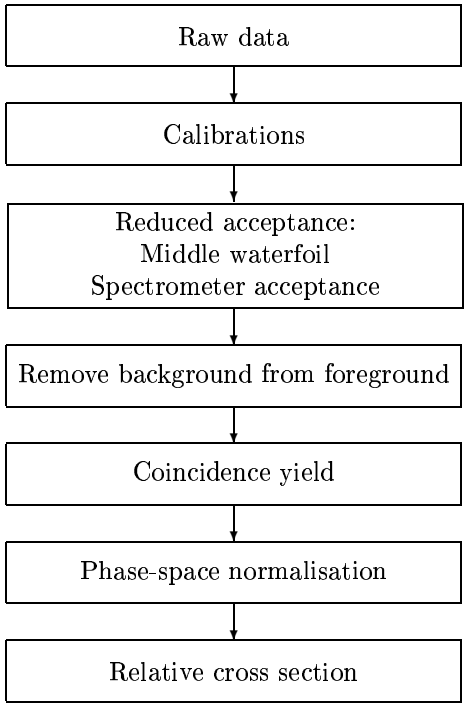

The data analysis proceeded via two basic steps: first, the ESPACE data acquisition/analysis software was used for event reconstruction and to produce HBOOKs[1], and second, PAW[2] was then used to study the contents of these HBOOKs in detail. In parallel, a plethora of normalisation data stored in ASCII text files was put into a MySQL database[3] for easy access.

The Event Scanning Program for Hall A Collaboration Experiments (ESPACE) was used to sort data, create histograms and calibrate experimental variables. It employed the same user interface as PAW and scanned the raw-data files, extracted and sorted the data, created ntuples[4] and wrote the results into HBOOK files. This was usually done through scripts according to the desire of the user, but ESPACE also had an interpreter that accepted direct commands. ESPACE required a number of input files that described the experimental set-up and kinematics in detail. One of these files was an ASCII text file known as the "database", which contained all the details describing the spectrometers. These details, such as the matrix elements describing the spectrometer magnets and the coefficients representing the behaviour of the various ADCs and TDCs, usually changed between experiments and were thus carefully checked and optimised for this measurement.

The Physics Analysis Workstation (PAW) was utilised to carefully examine the HBOOK data files. PAW is FORTRAN based, driven by macros, and had both a text interface and a Graphical User Interface (GUI). PAW is well known and widely used, but is gradually being replaced by ROOT[5].

3.2 Calibrations

As previously mentioned, calibration studies were performed to check and (if necessary) update the database representing the spectrometers and the detectors used in the ESPACE analysis. These included ADC (scintillator gain) calibrations, beta (scintillator TDC timing) calibrations, VDC t_0 (wire timing) calibrations and $y_{\rm tg}$ (reconstruction) calibrations.

ADC calibration: The scintillator PMT output pulses were not gain, attenuation or offset matched at the hardware level. Particles of the same energy thus produced output pulses of different amplitudes depending upon which scintillator paddle they passed through. The effects were removed from the

[1] HBOOK is a Fortran package for making histograms and fits. It has been in continuous development since the 1970s. For more information, see `http://wwwasdoc.web.cern.ch/wwwasdoc/hbook_html3/hboomain.html`.

[2] Physics Analysis Workstation (PAW) was conceived at CERN in 1986 as a tool for scientists to analyse and present their data. For more information, see `http://wwwasd.web.cern.ch/wwwasd/paw/`.

[3] MySQL is an open-source database server adhering to the ANSI standard Structured Query Language (SQL). For more infromation, see `http://www.mysql.com`.

[4] An ntuple is a data structure like a table with each row corresponding to an event and each column corresponding to a variable. Cuts can be applied to the variables and the results plotted in histograms.

[5] ROOT is a C++-based object-oriented interactive framework for analysing and presenting data. For more information, see `http://root.cern.ch/`.

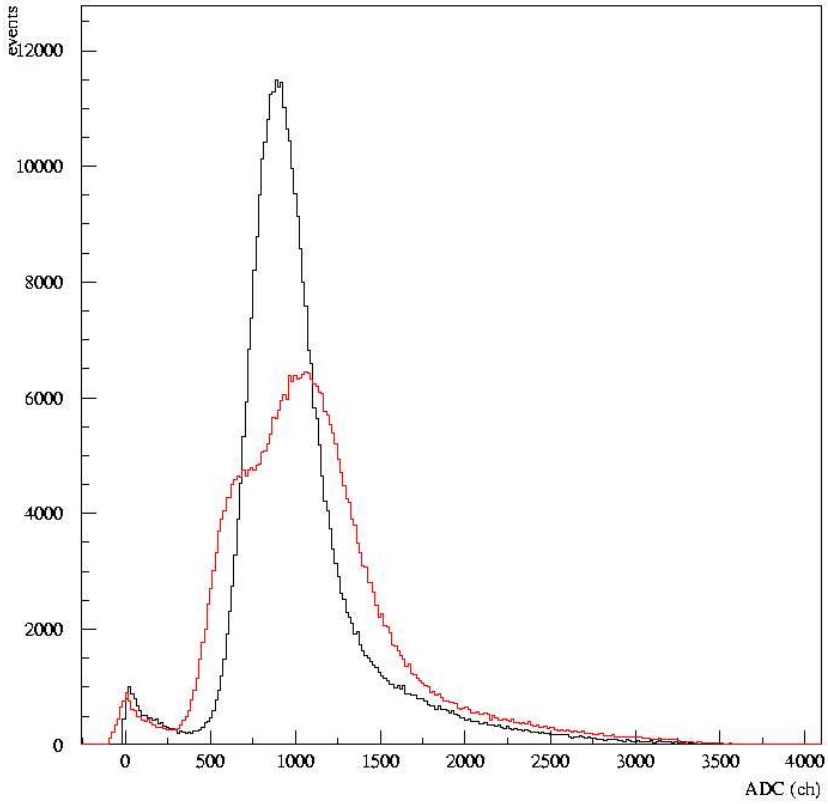

Figure 3.1: Sample commissioning left-arm ADC spectra from a single PMT before (red) and after (black) calibration. The x-axis (particle energy) is in units of ADC channels.

data using a software algorithm which matched the various distributions for quasimonoenergetic particles. See Figure 3.1 for comparisons.

Further, as the scintillator discriminators were not Constant-Fraction Discriminators (CFDs), the amplitude of the ADC output pulses affected the timing in the TDCs — a phenomenon commonly known as "time walk"[6]. A second software algorithm examined the correlations between the scintillator ADC and TDC data to align the timing without regard to the amplitude of the analog pulse. This was an important precursor to the beta calibration.

Beta calibration: Due to varying cable lengths and module processing times, scintillator pulses from the different trigger paddles took different amounts of time to be processed by the electronics. Hence, monoenergetic particles (i.e. particles with the exact same velocities) were assigned different TOF values depending on which combination of upstream and downstream

[6]Simply put, the larger the amplitude of the analog input pulse, the earlier the corresponding discriminator output pulse.

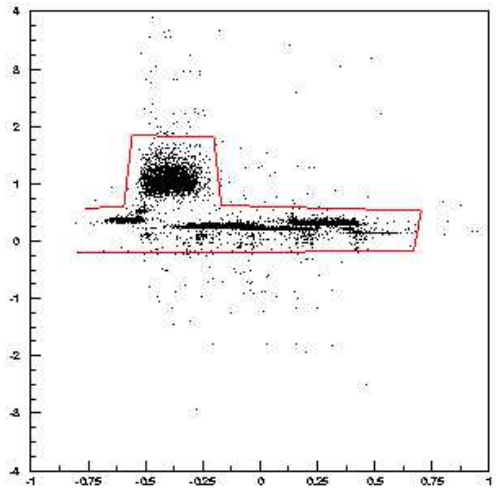

Figure 3.2: Sample raw proton β spectrum for the right spectrometer before calibration. On the x-axis is x_{rot} (in metres) representing the vertical position of the track at the scintillator plane. On the y-axis is the β of the proton. Six individual scintillator paddles can be seen, one of which has substantially different gain characteristics.

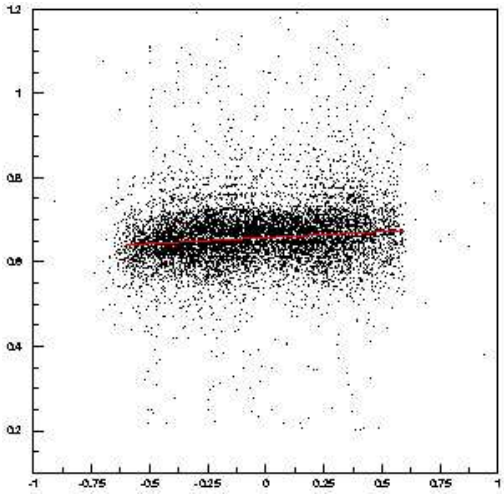

Figure 3.3: Sample proton β spectra after calibration. On the x-axis is x_{rot} (in metres) representing the vertical position of the track at the scintillator plane. On the y-axis is the β of the proton. Note that this scale is reduced considerably compared to that in Fig 3.2. The scintillator paddles are now indistinguishable and act as a single scintillator plate.

trigger scintillator paddles they passed through. This difference in timing made particle identification using TOF measurements less reliable. The variation was seen by plotting particle speed β ($\equiv v/c$) calculated from TOF versus vertical position in the focal plane (a variable called $x_{\rm rot}$; see Figure 3.2). Since the momentum and mass of the particles were known, the speed of the particles was calculated and offsets were assigned to each scintillator paddle to align the distributions at a single value (Figure 3.3).

VDC $\mathbf{t_0}$ calibration: This calibration matched the end point t_0 of the VDC drift time spectrum (see Figure 2.16) for each sense wire in the VDCs so that spectra from all the wires could be collected into a single spectrum in a meaningful fashion. Knowledge of t_0 was also used in the reconstruction algorithm.

$\mathbf{y_{tg}}$ calibration: $y_{\rm tg}$ was the horizontal position of the event vertex at the target as seen from a spectrometer. To calibrate $y_{\rm tg}$, a target consisting of seven thin carbon foils was used. The $y_{\rm tg}$ location of the foils was known from surveys and was reproduced in the calibration (see Figures 3.4 and 3.5)[7].

[7]The spectra generated from E00-102 data showed no improvement after the calibration; the reconstructed foils were already well aligned. The spectra in Figures 3.4 and 3.5 are from the E93-050 experiment [24] (also performed in Hall A) and have been included for completeness.

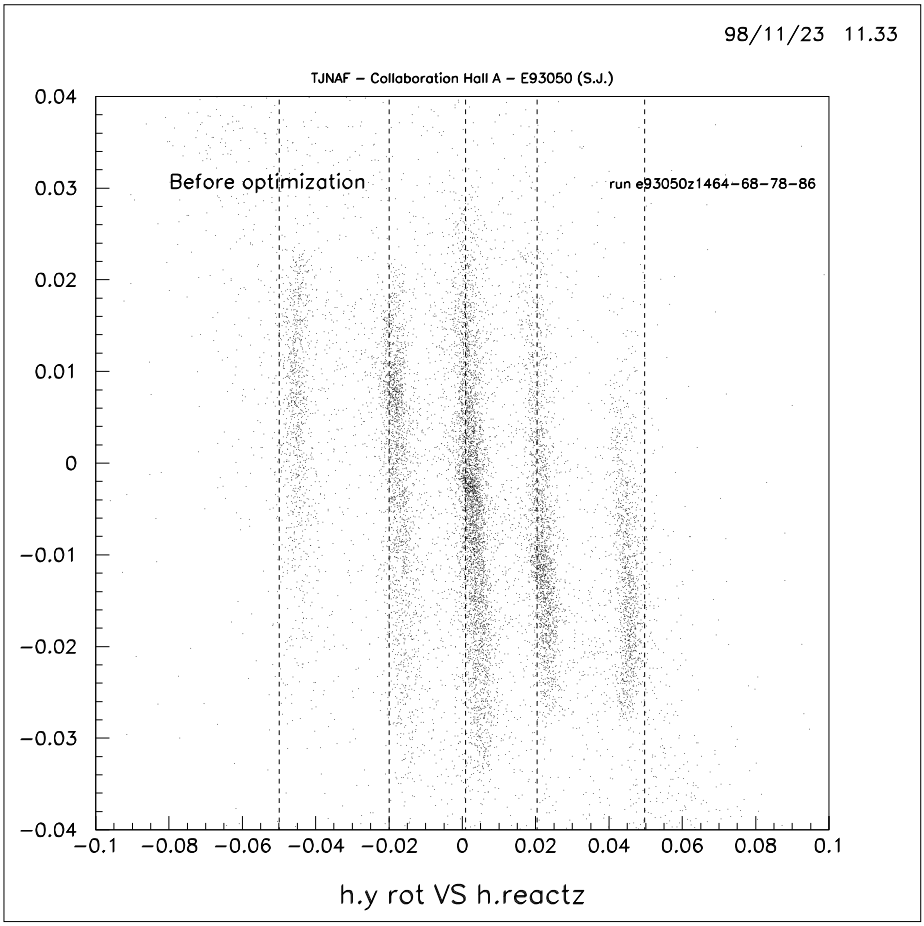

Figure 3.4: Sample spectrum [25] illustrating $y_{\rm tg}$ reconstruction before calibration. A 7-foil (of which five can be seen) ^{12}C target was used. On the x-axis is $h.reactz$ (also denoted Right Arm $z_{\rm react}$ and directly proportional to $y_{\rm tg}$) which is the reconstructed position (in metres) of the coincidence event vertex along the beam direction as seen from the HRS$_{\rm r}$. On the y-axis is $h.y\_rot$ (also denoted Right Arm $y_{\rm rot}$) representing the horizontal position (also in metres) of the particle track in the focal plane. The vertical dashed lines represent the positions where the ^{12}C foils were expected to be according to surveys.

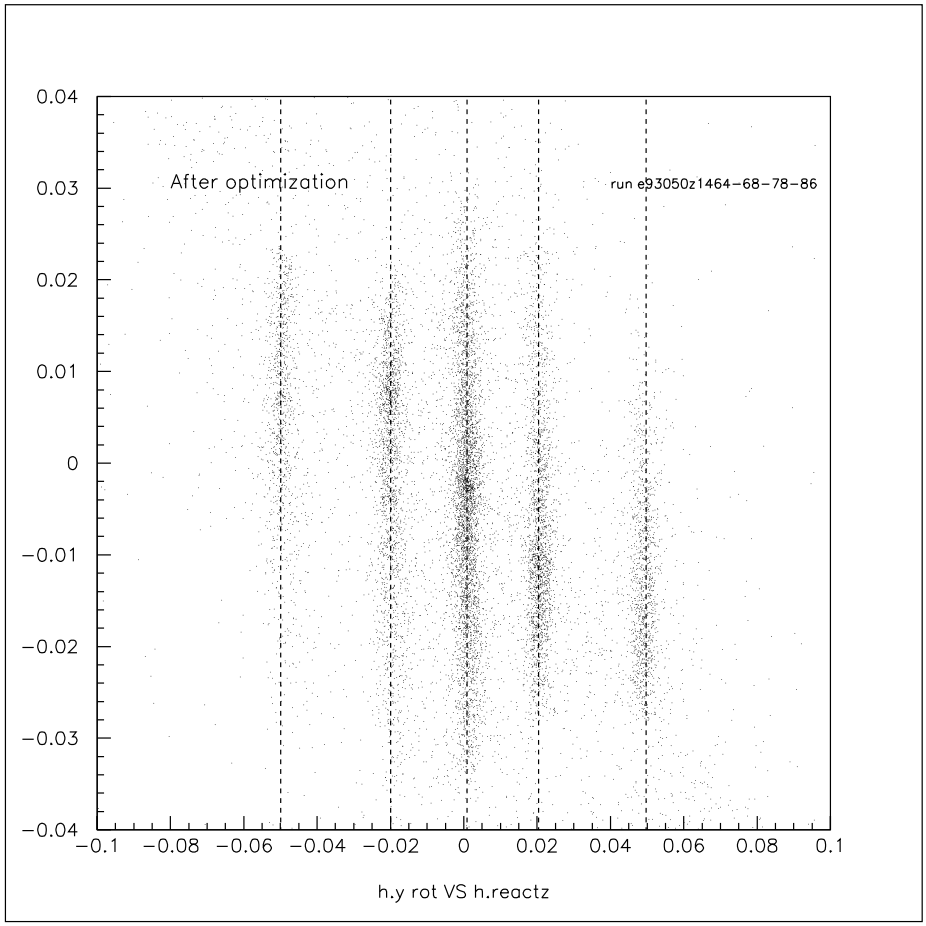

Figure 3.5: Sample spectrum [25] illustrating $y_{\rm tg}$ reconstruction after calibration. A 7-foil (of which five can be seen) ^{12}C target was used. On the x-axis is $h.reactz$ (also denoted Right Arm $z_{\rm react}$ and directly proportional to $y_{\rm tg}$) which is the reconstructed position (in metres) of the coincidence event vertex along the beam direction as seen from the HRS$_{\rm r}$. On the y-axis is $h.y\_rot$ (also denoted Right Arm $y_{\rm rot}$) representing the horizontal position (also in metres) of the particle track in the focal plane. The vertical dashed lines represent the positions where the ^{12}C foils were expected to be according to surveys.

3.3 Yield

In this section, the extraction of the yield for the $1p_{1/2}$ channel of the $^{16}\mathrm{O}(e,e'p)$ reaction is described.

3.3.1 Determining "Good" Runs

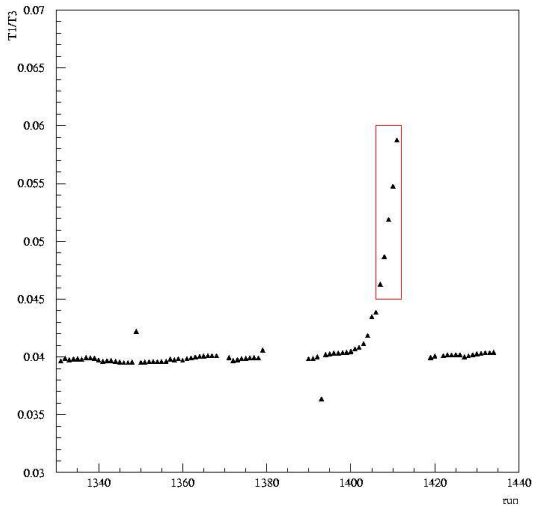

Figure 3.6: Example of how "bad" runs were rejected. The data are from kinematics G+. During this investigation, the waterfall target filled up with water. The proton rates (T1) increased while the electron rates (T3) decreased so that the quotient (T1/T3) rose rapidly. The red box shows which runs were judged to be "bad".

Subsequent to the calibrations described in the previous section, a first pass was made through the data examining the spectra from all of the detectors on a run-to-run basis. By comparing electron and proton event rates, defining average rates, and rejecting runs with event rates that deviated too much from the norm, a number of runs were labelled as "bad". These "bad" runs will require further data analysis beyond the scope of this thesis. For the remainder of this analysis, only runs with "normal" event rates were considered.

3.3.2 Data Reduction Cuts

The major step taken in analysing the good-data runs in this work was to examine only those events which passed through the centre of the spectrometer acceptances. This was because these events were in general more straightforward to analyse as their trajectories were much simpler. Cuts on events originating from the middle waterfoil and on the reconstructed in-plane and out-of-plane electron and proton trajectory angles were used to accomplish this task.

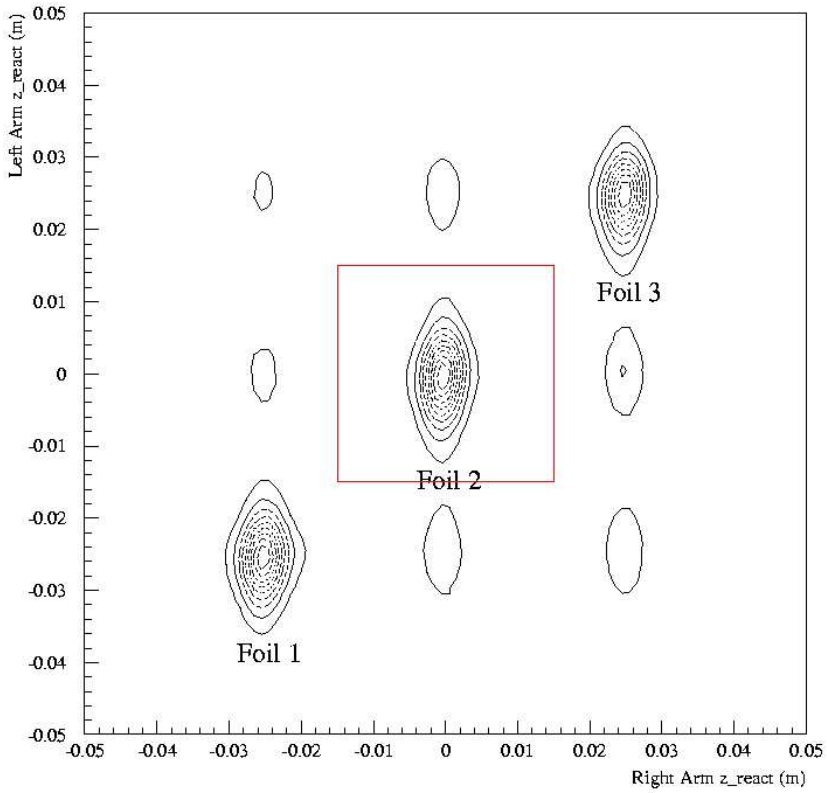

Figure 3.7: An illustration of the cut on the middle waterfoil. Left Arm z_{react} and Right Arm z_{react} are the reconstructed positions of the coincidence event vertex along the beam direction as seen from the respective arm, with the origin of the coordinate system corresponding to the centre of the Hall. The three distributions along the diagonal in the figure correspond to events from the three waterfoils where both the electron and the proton have been reconstructed to have come from the same foil. The other six, smaller, off-diagonal elements come from random coincidences between events where the electron has come from a different foil than the proton. The difference in reconstruction accuracy (that is, the widths of the distributions) between the right and the left spectrometer arm is a trigonometric effect. The waterfall separation was better when reconstructed by the right arm because the $\mathrm{HRS_r}$ was at a larger laboratory angle with respect to the beam direction. The red box shows how the middle foil was selected. The data is from A+ kinematics.

Middle Waterfoil

The middle waterfoil was located at the centre of the Hall and was thus in the middle of the acceptance[8] of the spectrometers. A cut was placed on the

[8]This assumes no significant spectrometer mispointing.

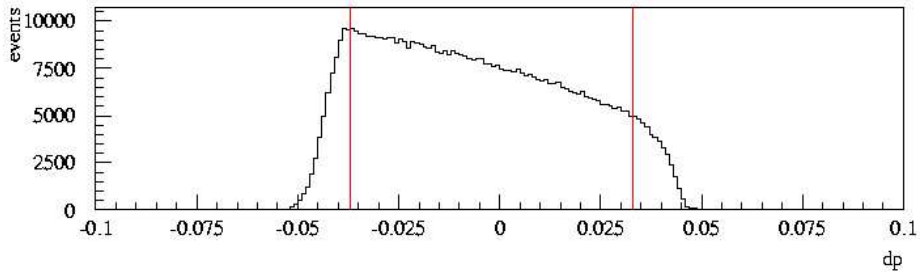

Figure 3.8: An illustration of the right arm spectrometer relative momentum acceptance cuts. The red lines indicate the cuts made in dp so that the only particles analysed were in the central acceptance region of the spectrometer. The general slope down towards the right was due to the smaller cross section at higher momentum. The data is from A+ kinematics.

	$\theta_{\rm tg}$ (rad)	$\phi_{\rm tg}$ (rad)	dp
$\rm HRS_l$	$-0.050 < \theta_{\rm tg} < 0.045$	$-0.026 < \phi_{\rm tg} < 0.024$	$-0.037 < dp < 0.033$
$\rm HRS_r$	$-0.045 < \theta_{\rm tg} < 0.045$	$-0.022 < \phi_{\rm tg} < 0.022$	$-0.037 < dp < 0.033$

Table 3.1: A summary of the acceptance cuts. $\theta_{\rm tg}$ ($\phi_{\rm tg}$) is the reconstructed vertical (horizontal) angle at the target between the particle trajectory and the ideal trajectory through the centre of the spectrometer acceptance. dp is the deviation of the momentum of the particles from the spectrometer central momentum, with positive values higher than central values.

reconstructed location of the coincidence-event vertex along the beam direction and the relative momentum in order to select only those events originating from the central waterfoil. In this manner, events originating from the upstream and downstream waterfoils were removed from the data set. See Figures 3.7 and 3.8 for details.

Trajectory Angles

In the outer reaches of the spectrometer acceptances, the relative spectrometer acceptance falls off as events are physically prevented from reaching the detectors by the magnet apertures, for example. For this work, a cut was applied to the data so that only events which had a completely unobstructed path through the spectrometers were considered. This reduced the spectrometer acceptance from the design values in Table 2.2 to the values in Table 3.1 (see Figures 3.9 and 3.8).

3.3.3 Timing and Coincidence Yield

The Coincidence Time-Of-Flight (CTOF) spectrum is typically used to quantify the number of random coincidences within the prompt timing peak. However, in this experiment, some real events were lost from the CTOF peak due to mis-timing (see Figure 3.10). Using the scaler redundancy in the spectrometers[9], two complementary CTOF spectra were created (one for each arm) with opposite

[9]Both spectrometers were instrumented with TDCs to make complementary CTOF spectra. Hence there was one CTOF spectrum created in each spectrometer arm. They were created with a local start and stopped by a trigger accepted by the opposite spectrometer.

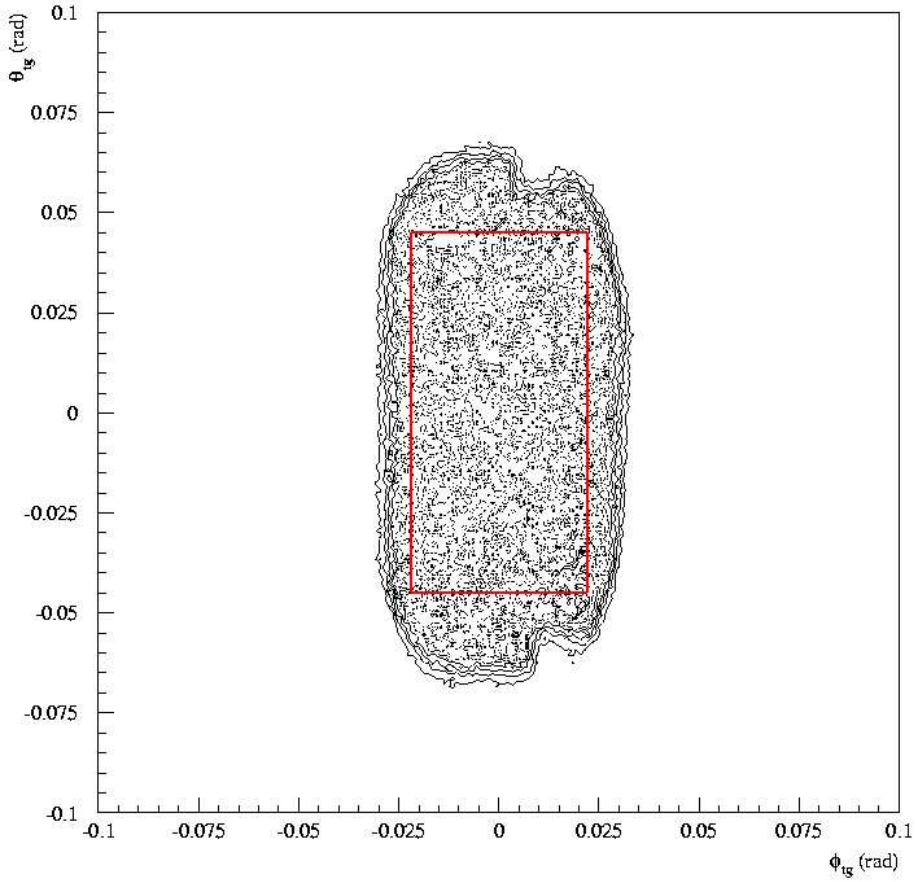

Figure 3.9: An illustration of the right arm spectrometer angular-acceptance cuts. Left arm angular-acceptance cuts were almost identical (see Table 3.1). The red box indicates the cuts made in $\theta_{\rm tg}$ and $\phi_{\rm tg}$ so that only the particles detected in the central acceptance region of the spectrometer were analysed. The lack of events in the upper and lower right-hand corners of the scatter plot was due to trajectory masking caused by the NMR probes in the spectrometer dipole magnet. The data is from A+ kinematics.

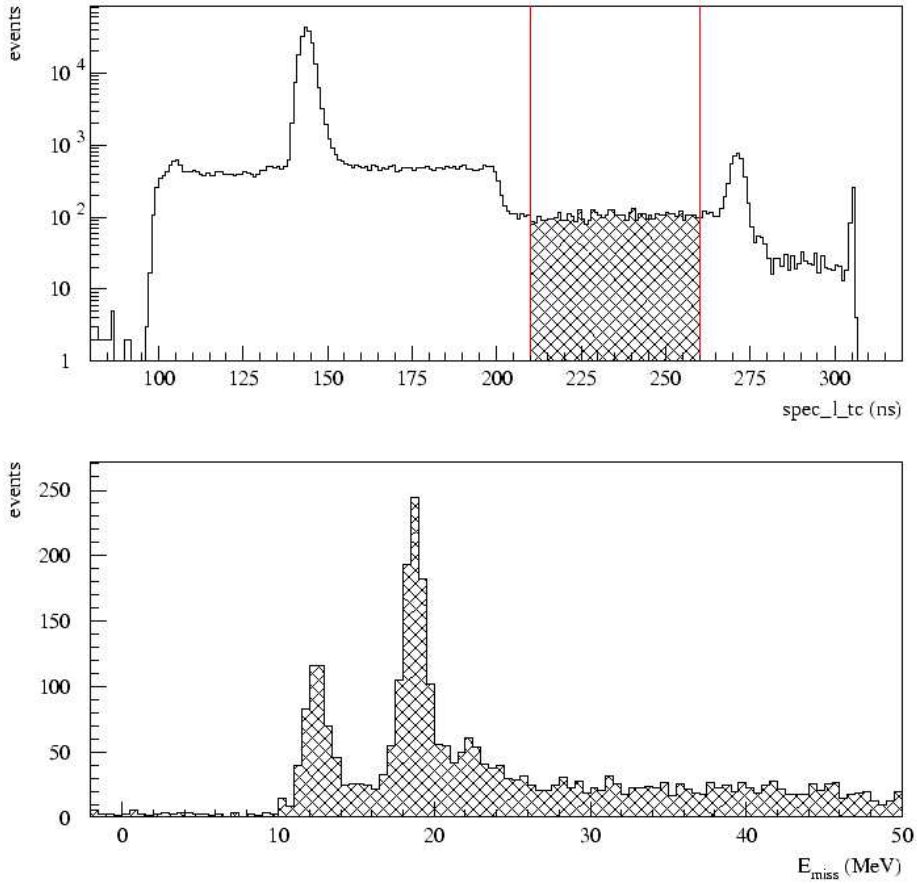

Figure 3.10: An illustration of mistiming in the coincidence time-of-flight determined by the HRS_e. The top panel shows that there were events with CTOF values outside the CTOF window; that is, the events with 200 ns $< spec\_l\_tc <$ 305 ns . The bottom panel shows an $E_{\rm miss}$ spectrum corresponding to events in the CTOF region marked with red in the top panel. There are clearly some real events as best evidenced by the peaks at 12.1 and 18.4 MeV corresponding to proton knockout from the $1p_{1/2}$ and $1p_{3/2}$ states of ^{16}O. These peaks would not appear if the events were purely random. The data is from A+ kinematics.

start and stop. The mistiming was clearly different in the two spectra (see Figure 3.11), and this information was used to determine how many real events were mistimed. The events with the anticipated timing are all in Region A. All other events were mistimed. To compensate for this problem, the number of real events outside Region A (that is, the number of events in Region $\bar{\rm A}$) was quantified for each kinematics, and correction factors determined.

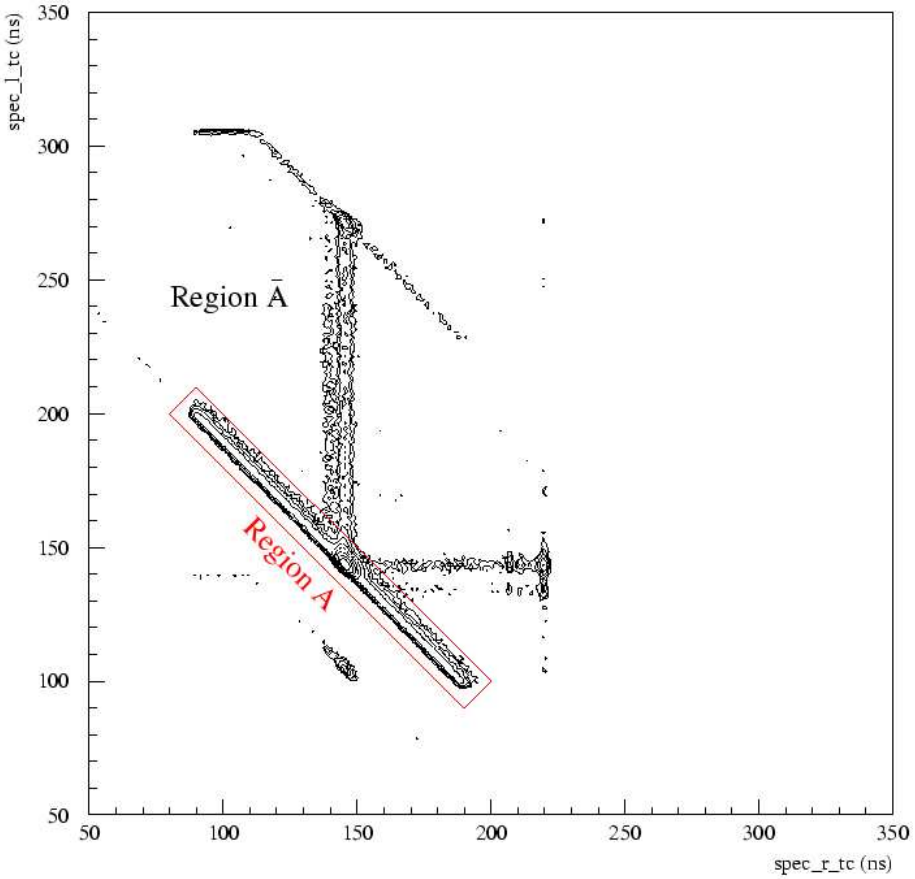

Figure 3.11: Coincidence time-of-flight scatterplot generated from the two spectrometers. Real events were mistimed in each arm. On the x-axis, $spec\_r\_tc$ was the CTOF value generated in the right arm, with a right arm scintillator signal as a start signal and a left arm accepted trigger as a stop signal. On the y-axis, $spec\_l\_tc$ was the CTOF value generated in the left arm, with a left arm scintillator signal as a start signal and a right arm accepted trigger as a stop signal. The events that had the anticipated timing fell within the Region A polygon. Events outside the Region A polygon were mistimed. These mistimed events amount to roughly 10% of the total yield. The data is from A+ kinematics.

Region A

Looking only at the events in Region A, a plot was made of $spec\_r\_tc - spec\_l\_tc$ (Figure 3.12). The number of events in the foreground region and in the background regions were determined. The foreground yield consisted of both real and random-coincidence events. The background yield consisted entirely of random-coincidence events. The total number of real events Y_{real} was

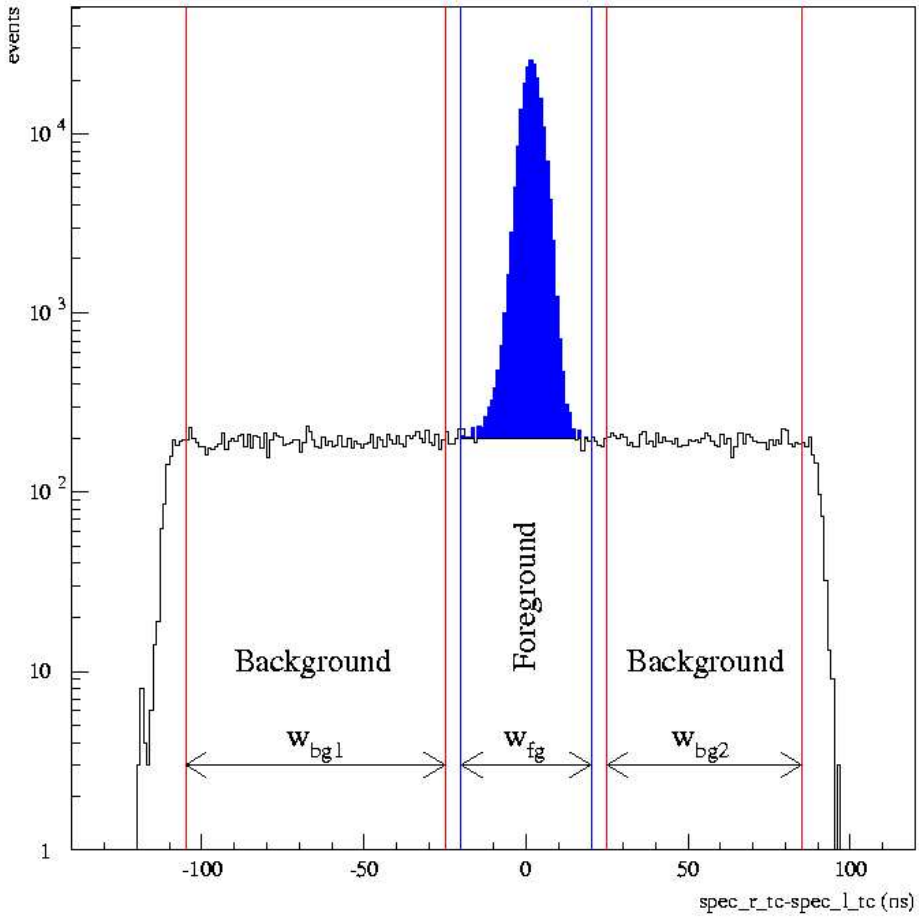

Figure 3.12: CTOF spectrum for Region A. The foreground region is 40 ns wide and includes both real and random events. The two background regions contain only random events, and together span 140 ns. The blue area is the prompt peak consisting entirely of real events. The data is from A+ kinematics.

calculated by subtracting the weighted background from the foreground (see Table 3.2). The weight was the size of the TDC interval used for the foreground divided by the total width of the TDC intervals used for the background.

$$
\begin{aligned}
Y_{\mathrm{real}} &= Y_{\mathrm{fg}} - (\mathrm{weight}) \cdot Y_{\mathrm{bg}} \\
&= Y_{\mathrm{fg}} - \left(\frac{w_{\mathrm{fg}}}{w_{\mathrm{bg1}} + w_{\mathrm{bg2}}} \right) \cdot Y_{\mathrm{bg}} \qquad (3.1)
\end{aligned}
$$

Here, Y_{fg} was the sum of the events in the foreground region, and Y_{bg} was the sum of the events in the background regions. w_{fg}, w_{bg1} and w_{bg2} were the widths of the respective TDC intervals.

Kinematics	Foreground events Region A	Background events Region A	Real events Region A
A+	189852	22059	183549
C+	243119	42618	230942
D+	132178	32937	122767
E+	123126	46534	109831
F+	241399	202966	183409

Table 3.2: Region A CTOF background subtraction using the CTOF intervals defined in Figure 3.12. Note that all $^{16}\mathrm{O}(e,e'p)$ channels are represented. The number of real events was calculated using Equation 3.1 with a weight of $40/140 = 0.285714$.

Region $\bar{\mathrm{A}}$

To determine the number of real events located outside Region A due to mistiming, the E_{miss} spectrum for those events was used (see Figure 3.13). The E_{miss} spectrum consisted of real events superimposed upon a random-coincidence background. The number of random coincidences was determined with a linear fit in the non-physical range -70 MeV $< E_{\mathrm{miss}} <$ 10 MeV where there were no peaks. The number of random coincidences in the region $E_{\mathrm{miss}} > 10$ MeV was determined by extrapolating the fit function. The total number of real events lying outside Region A was then determined by subtracting the fitted function from the data, and summing the resulting distribution of events for $10 < E_{\mathrm{miss}} < 150$ MeV.

Real Events

The number of real events inside Region A and the number of real events outside Region A were hence determined and the mistiming was corrected for based upon this ratio according to

$$
\begin{aligned}
Y_{\mathrm{real,cor}} &= \left(1 + \frac{Y_{\mathrm{real},\bar{\mathrm{A}}}}{Y_{\mathrm{real,A}}} \right) \cdot \tilde{Y}_{\mathrm{real,A}} \\
&= K \cdot \tilde{Y}_{\mathrm{real,A}}. \qquad (3.2)
\end{aligned}
$$

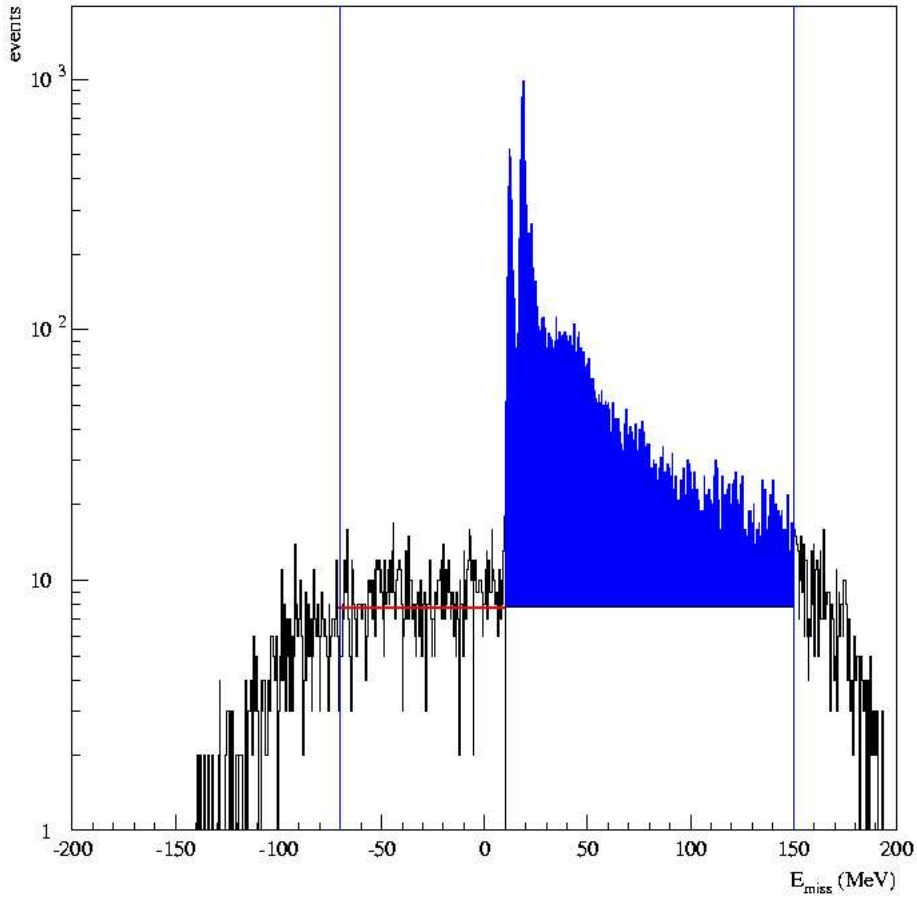

Figure 3.13: $E_{\rm miss}$ spectrum for Region $\bar{\rm A}$. The fall-off of the reconstructed $E_{\rm miss}$ distribution at large values was caused by the limits of the spectrometer acceptance. The region inside the blue lines is where the random-coincidence background was assumed to be flat. The red line is a linear fit to the background that was extrapolated for $10 < E_{\rm miss} < 150$ MeV and used for subtracting the background. The data is from A+ kinematics.

Here, $Y_{\rm real,A}$ was the real yield from Region A, $Y_{\rm real,\bar{A}}$ was the real yield from Region $\bar{\rm A}$ and $Y_{\rm real,cor}$ was the corrected real yield. $\tilde{Y}_{\rm real,A}$ was the real yield (from Region A) which belonged to the interval of $E_{\rm miss}$ that was studied. This algorithm assumed that the $E_{\rm miss}$ distributions were the same in Region $\bar{\rm A}$ as in Region A; that is, all real events had the same probability of being mistimed. Preliminary investigations indicated that this assumption was valid. The correction factors for the lost events are presented in Table 3.3.

Kinematics	All events Region $\bar{\text{A}}$	Background events Region $\bar{\text{A}}$	Real events Region $\bar{\text{A}}$
A+	20046	3430	16616
C+	29864	6904	22960
D+	18128	5460	12668
E+	19188	7828	11360
F+	54269	34923	19346

Table 3.3: Region $\bar{\text{A}}$ background subtraction. A linear fit to the non-physical region in the E_{miss} spectrum was made and the background was parametrised by extrapolating this fit function over the entire E_{miss} range (see Figure 3.13). The number of real events was calculated by summing the fitted function and the spectrum, separately, over this E_{miss} range and subtracting the former from the latter.

Kinematics	Real events Region A	Real events Region $\bar{\text{A}}$	Correction factor K
A+	183549	16616	1.091
C+	230942	22960	1.099
D+	122767	12668	1.103
E+	109831	11360	1.103
F+	183409	19346	1.105

Table 3.4: Table of mistiming correction factors K defined in Equation 3.2. The real events were integrated for $10 < E_{\text{miss}} < 150$ MeV. Region A (see Figure 3.11) yield results were scaled by K to correct for mistiming.

3.3.4 $1p_{1/2}$ State

The top and middle panels in Figure 3.14 are $E_{\rm miss}$ spectra created based upon the CTOF cuts shown in Figure 3.12. The top panel was created from foreground events, while the middle spectrum was created from background events. The background distribution was weighted by the ratio of the CTOF gates as per Equation 3.1 and subtracted from the foreground distribution on a bin-by-bin basis, resulting in the real yield shown in the bottom panel. This distribution was summed for $10 < E_{\rm miss} < 16$ MeV. The result was the $1p_{1/2}$-state yield.

3.4 Cross Section

3.4.1 Absolute Cross Section

The six-fold differential cross section for the $^{16}{\rm O}(e,e'p)$ reaction can be written (recall Equation 1.1) as

$$\frac{d^6\sigma}{d\Omega_{\rm e}d\omega d\Omega_{\rm p}dE_{\rm p}} = \frac{R}{(L\cdot\epsilon_{\rm e})(\epsilon_{\rm p}\cdot\epsilon_{\rm coin})}\left(\frac{Y_{\rm real}}{\Delta V}\right), \tag{3.3}$$

where $\epsilon_{\rm e}$, $\epsilon_{\rm p}$ and $\epsilon_{\rm coin}$ were the efficiencies involved with registering electron, proton and coincidence events; L was the luminosity, which was the product of the beam charge and the target thickness; $Y_{\rm real}$ was the yield; ΔV was the volume of the phase space that was populated; and R was a correction applied to account for events that had radiated in or out of this phase-space volume (see footnote 10).

3.4.2 Relative to H(e,e)

Equation 3.3 is in general valid for all kinematics, regardless of how the various kinematic variables and spectrometer settings relate to each other. In this experiment, the electron spectrometer was static in both field and angle. Further, the proton spectrometer was static in field. The constant spectrometer fields together with identical angular and momentum acceptance cuts used for all kinematics in this analysis resulted in identical efficiencies and phase-space volumes for all kinematics. Equation 3.3 was thus rewritten as

$$\sigma_{^{16}{\rm O}(e,e'p)} = \mathcal{C}\cdot\frac{R_{^{16}{\rm O}(e,e'p)}\cdot Y_{^{16}{\rm O}(e,e'p)}}{L}, \tag{3.4}$$

where $\mathcal{C}$ was a constant representing all the variables that were identical in each kinematical setting, and L was the luminosity (the product of the integrated beam current and the effective thickness of the waterfall target). $R_{^{16}{\rm O}(e,e'p)}$ was the radiative correction for $^{16}{\rm O}(e,e'p)$.

As stated earlier, the effective target thickness was unknown so that L was unknown. However, since the electron spectrometer was static throughout the

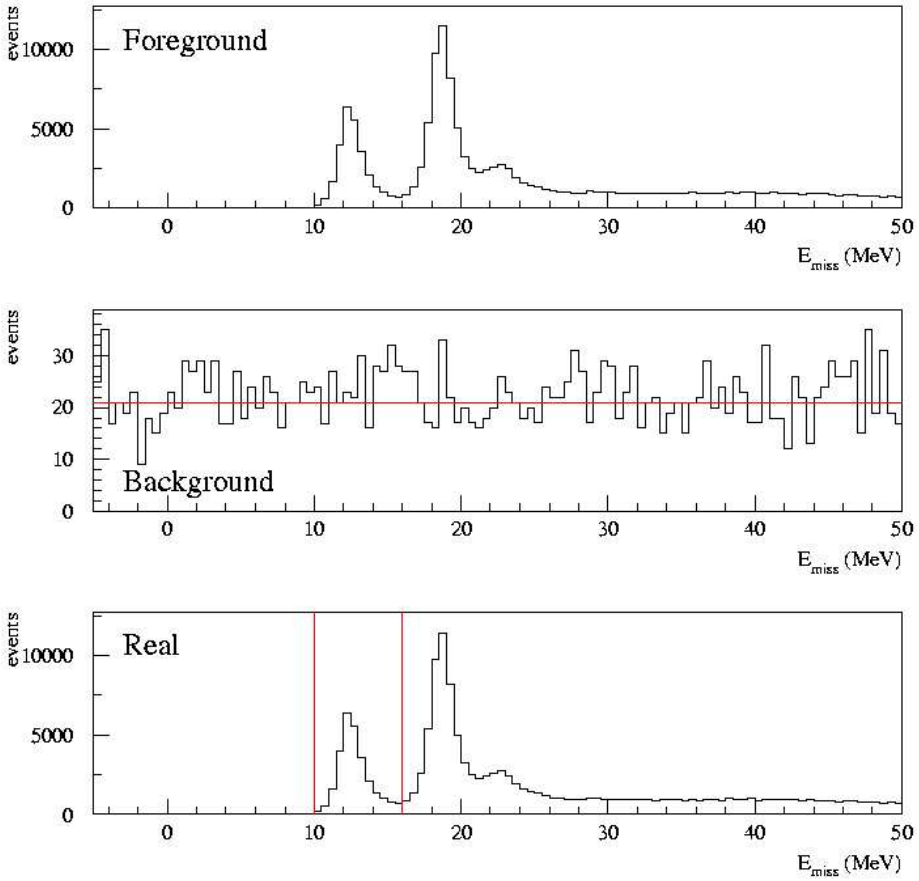

Figure 3.14: An illustration of the background subtraction in $E_{\rm miss}$ space. The top panel shows the $E_{\rm miss}$ spectrum generated from the foreground events which contains both real and random events. The middle panel was generated from the background regions. The distribution is clearly flat, which is consistent with a purely random distribution. The bottom panel resulted from subtracting the (weighted – see Equation 3.1) background distribution shown in the middle panel from the foreground distribution in the top panel. These events are real events. From the left, the first peak in the $E_{\rm miss}$ spectrum delineated by the vertical red lines corresponded to the knock-out of one of the $1p_{1/2}$ protons from ^{16}O. The data is from A+ kinematics.

entire experiment, it simultaneously measured a constant ^{1}H(e,e) cross section in addition to the ^{16}O$(e,e'p)$ cross section, namely

$$\sigma_{^1\mathrm{H}(e,e)} = \mathcal{C}' \cdot \frac{R_{^1\mathrm{H}(e,e)} \cdot Y_{^1\mathrm{H}(e,e)}}{L}, \tag{3.5}$$

where $\mathcal{C}'$ was a constant representing all the variables that were constant in each kinematical setting, L was again the luminosity, $R_{^1\mathrm{H}(e,e)}$ was the radiative

correction for $^1\mathrm{H}(e,e)$, and $Y_{^1\mathrm{H}(e,e)}$ was the number of scattered (and detected) electrons.

A relative value of the $^{16}\mathrm{O}(e,e'p)$ cross section was thus obtained by normalising the $^{16}\mathrm{O}(e,e'p)$ results to the $^1\mathrm{H}(e,e)$ results according to

$$\sigma_{\mathrm{relative}} = \frac{\sigma_{^{16}\mathrm{O}(e,e'p)}}{\sigma_{^1\mathrm{H}(e,e)}} = \frac{\mathcal{C}}{\mathcal{C}'} \cdot \frac{R_{^{16}\mathrm{O}(e,e'p)}}{R_{^1\mathrm{H}(e,e)}} \cdot \frac{Y_{^{16}\mathrm{O}(e,e'p)}}{Y_{^1\mathrm{H}(e,e)}} \propto \frac{Y_{^{16}\mathrm{O}(e,e'p)}}{Y_{^1\mathrm{H}(e,e)}}, \qquad (3.6)$$

where the constants $\mathcal{C}$ and $\mathcal{C}'$ as well as the radiative corrections $R_{^1\mathrm{H}(e,e)}$ and $R_{^{16}\mathrm{O}(e,e'p)}$[10] have been collected into the proportionality. $Y_{^1\mathrm{H}(e,e)}$ was given by the $\mathrm{HRS_l}$ electron-singles scaler. In this manner, knowledge of the target thickness became unnecessary.

3.4.3 Phase-Space Normalisation

The background-subtracted p_{miss} spectrum obtained from the data (see the top panel of Figure 3.15) was then normalised on a bin-by-bin basis using a simulated p_{miss} spectrum for purely random events to account for phase-space effects (see the middle panel of Figure 3.15). Note that the exact same cuts applied to the actual data were applied to the simulated data. The result is the relative cross section for $^{16}\mathrm{O}(e,e'p)$ (see the bottom panel of Figure 3.15).

3.4.4 p_{miss}-binning

Systematical uncertainties in the data were estimated to be in the order of 5% [26]. If the data were binned such that only a single data point resulted from each kinematics, the statistical uncertainties would be significantly smaller than 5%. There were hence enough data to divide each kinematics into subsets and maintain statistical uncertainties of approximately 5%. This gave a better view of how the cross section varied with p_{miss}. It also showed the overlap between the kinematics due to the spectrometer acceptance.

The relative cross section for $^{16}\mathrm{O}(e,e'p)$ is shown in Figure 3.16.

3.4.5 Summary

The relative cross section for the removal of $1p_{1/2}$-state protons from $^{16}\mathrm{O}$ using the $(e,e'p)$ reaction for $70 < p_{\mathrm{miss}} < 320$ MeV/c was extracted by performing the following steps:

[10] As shown in Figure 3.14, the E_{miss} peaks were not symmetric about the proton-removal energy, but instead had a long tail extending towards higher E_{miss}. This effect was due to radiation. Simply put, the electron radiated photons both upstream and downstream of the interaction vertex. In each case, energy was lost to the reconstruction algorithm and a higher E_{miss} was reconstructed, giving rise to the long tail observed. Precise evaluation of the radiative effects (standard but time consuming calculations in this type of data analysis) was judged to be beyond the scope of this thesis. However, since the electron spectrometer was static in both field and angle, the electron radiative effects were the same in all kinematics. Thus, it was reasonable to collect them into the proportionality in Equation 3.6.

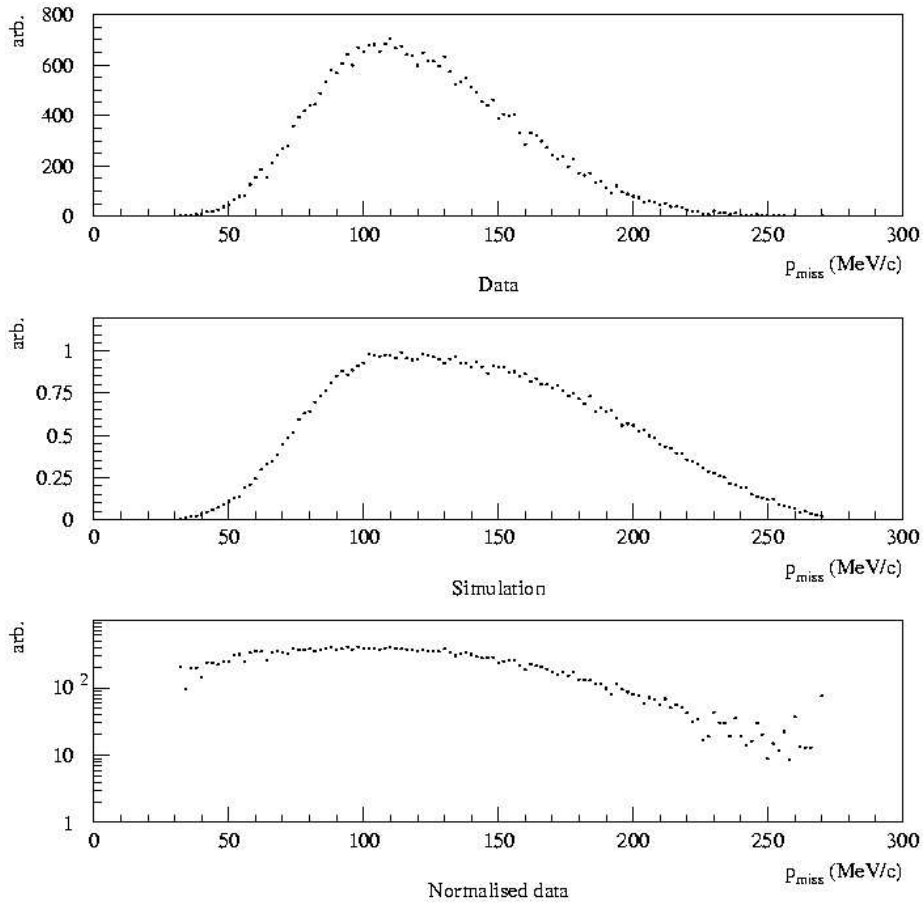

Figure 3.15: Illustration of the phase-space normalisation procedure. The top panel is a $p_{\rm miss}$ spectrum of real events generated from data in A+ kinematics. The middle panel shows the simulated phase-space distribution; that is, how the spectrum would look if populated completely at random. The shape of the phase-space spectrum was due to the cuts imposed in the data analysis. The bottom panel shows the result: a phase-space normalised $p_{\rm miss}$ spectrum. The bin width is 1 MeV/c. Statistical uncertainties have been omitted for clarity.

1. Apply cuts on $\phi_{\rm tg}$, $\theta_{\rm tg}$, $z_{\rm react}$, CTOF Region A and $E_{\rm miss}$ (see Section 3.3.2).
2. Subtract background bin-by-bin (see Section 3.3.3).
3. Apply mistiming correction factor (see Table 3.4).
4. Normalise to luminosity (see Equation 3.6 and Table 3.6).
5. Normalise to phase-space (see Section 3.4.3 and Appendix D).
6. Divide each data point by the $p_{\rm miss}$ binwidth (see Table 3.5).

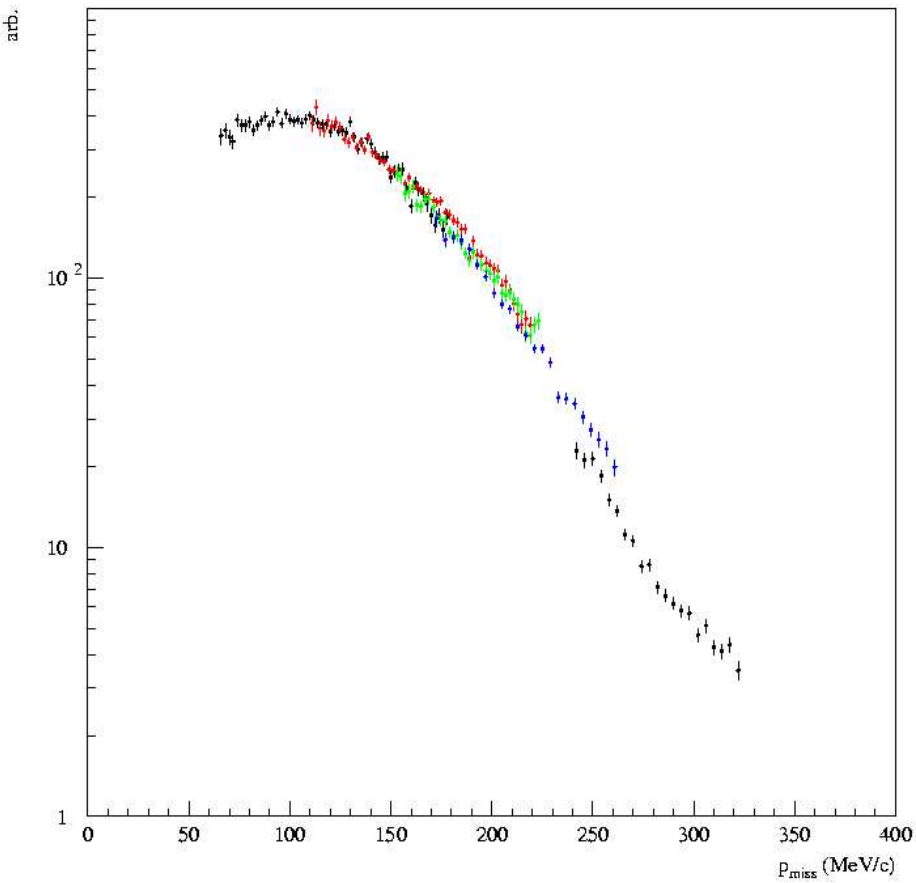

Figure 3.16: The relative cross section for the removal of $1p_{1/2}$-state protons from ^{16}O using the $(e, e'p)$ reaction for $70 < p_{\mathrm{miss}} < 320$ MeV/c. Each kinematics has been assigned a colour (black for A+; red for C+; green for D+; blue for E+; and black again for F+). A p_{miss} bin width of 2 MeV/c was used for A+, C+ and D+, while 4 MeV/c bins were used for E+ and F+. The uncertainties shown are statistical. Data points with statistical uncertainty larger than 7% were omitted for clarity. The systematic uncertainties are estimated to be on the order of 5% [26].

Kinematics	p_{miss} binwidth (MeV/c)
A+	2
C+	2
D+	2
E+	4
F+	4

Table 3.5: Table of p_{miss} binwidths used for the various kinematics displayed in Figure 3.16.

Kin.	Electron events	Norm. factor
A+	900590486	0.900590486
C+	2080036512	2.080036512
D+	1840134074	1.840134074
E+	2980240442	2.980240442
F+	17222733463	17.222733463

Table 3.6: The total number of electron events for each kinematics. The number of electron events is proportional to the electron beam intensity and the target thickness.

Chapter 4

Results

4.1 RDWIA Ingredients

Recall the presentation of DWIA presented in Section 1.3.2. While it is beyond the scope of this thesis to evaluate in detail the components of the theoretical calculations, it is possible to discuss the basic concepts behind these ingredients. The interested reader is directed to [13] for more detail.

The calculations addressed six primary topics. These included:

- **Relativity:** The beam electrons were ultra-relativistic, and thus relativistic effects were considered.
- **The Coulomb Interaction:** As the electron probe and the target nucleus were charged, Coulomb distortions of the incoming electron beam (which resulted in an effective momentum transfer q_{eff}) were addressed.
- **The Bound-Nucleon Wave Function:** The proton occupied a bound state within the oxygen nucleus. The NLSH bound-nucleon wave function [27] was employed to describe the momentum distribution.
- **The Proton Form Factor:** Rather than explicitly accounting for sub-nucleonic degrees of freedom, the internal structure of the proton was treated phenomenologically with the GK nucleon form-factor model [28].
- **The Current Operator:** An operator was necessary to describe the nuclear current which "connected" the initial and final states. Current operators CC1 and CC2 [29] were used.
- **The Optical Potential:** After being struck, the knocked-out proton interacted with the residual ^{15}N nucleus. This interaction was described phenomenologically by the EDAI-O optical potential [30], the parameters of which were determined from complementary proton-scattering data from ^{16}O.

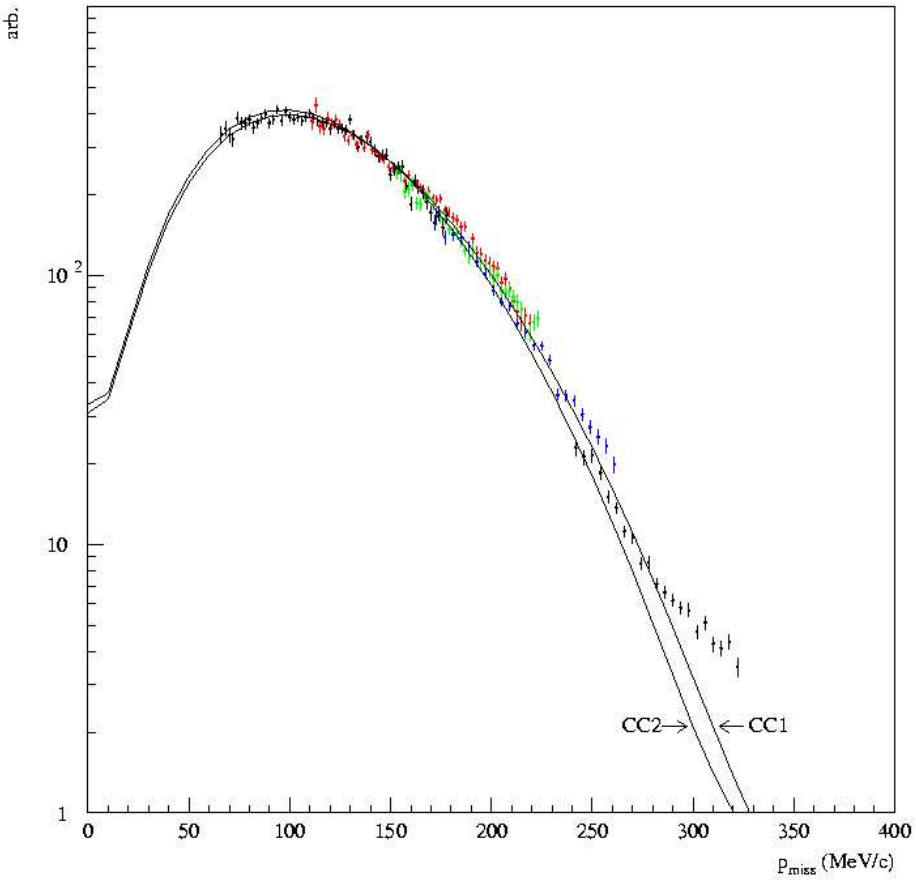

Figure 4.1: Relative cross-section data for $1p_{1/2}$-proton removal from ^{16}O using the $(e, e'p)$ reaction compared to the Relativistic Distorted-Wave Impulse Approximation (RDWIA) calculations of Udías *et al.* [31]. See text for details.

Recall that the effects of varying the bound-nucleon wave function, the current operator and the optical potential were shown in Figure 1.9.

Relative cross-section data for $1p_{1/2}$-proton removal from ^{16}O using the $(e, e'p)$ reaction are presented in Figure 4.1. The data are identical to those shown in Figure 3.16. The curves labeled CC1 and CC2 are Relativistic Distorted-Wave Impulse Approximation (RDWIA) calculations of Udías *et al.* [31]. The normalisation is arbitrary. As previously mentioned, both calculations had as input the NLSH bound-nucleon wave function [27], the GK form-factor model [28] and the purely phenomenological EDAI-O optical potential [30]. The current operator was changed from CC1 to CC2.

The calculations shown in Figure 4.1 are in very reasonable agreement with the data resulting from the analysis described in Chapter 3 for $70 < p_{\mathrm{miss}} < 225$ MeV/c.

4.2 Conclusion

A $70 < p_{\mathrm{miss}} < 320$ MeV/c subset of the $-515 < p_{\mathrm{miss}} < 725$ MeV/c complete data set from the Jefferson Lab Hall A experiment E00-102 has been examined for proton knock-out from the $1p_{1/2}$ state of ^{16}O. The agreement between the analysed data and theoretical calculations has been found to be very promising.

A more detailed analysis is warranted. All indications are that this dataset is the benchmark for $(e, e'p)$ from a "heavy" nucleus.

Appendix A

MySQL Database

A MySQL database has been created. This was accomplished using Perl scripts which scanned and sorted normalisation and scaler history information for each run and inserted it into the database. The database has more than 180 entries for each run. An overview and introduction to the database can be seen at `www.jlab.org/~mattias`. Note that this database is separate from the database used by ESPACE, which is only an ASCII text file.

```
mysql> show tables;
+------------------+
| Tables_in_e00102 |
+------------------+
| B_ENERGY         |
| E_SETUP          |
| H_SETUP          |
| RUN              |
| TARGET           |
+------------------+
5 rows in set (0.00 sec)
```

Figure A.1: Sample MySQL code. The table `B_ENERGY` contained general information about the beam, `E_SETUP` and `H_SETUP` contained information about the setup of the HRS_l and HRS_r, respectively, and `TARGET` contained information about the targets that were used. `RUN` contained information specific to each run.

```
mysql> select run_num, length, events, comment from RUN where
    -> comment like "%KIN A+%";
+---------+------------+---------+---------+
| run_num | length     | events  | comment |
+---------+------------+---------+---------+
|    1311 | 14.4280005 | 1002266 | KIN A+  |
|    1312 | 12.8490000 | 1005672 | KIN A+  |
|    1313 | 17.0130005 | 1000952 | KIN A+  |
|    1314 | 14.3719997 | 1003859 | KIN A+  |
|    1315 | 15.9650002 | 1003945 | KIN A+  |
|    1316 | 18.1280003 | 1003367 | KIN A+  |
|    1319 | 19.3980007 | 1001584 | KIN A+  |
|    1320 | 18.9580002 | 1002144 | KIN A+  |
|    1321 | 17.1250000 | 1002413 | KIN A+  |
|    1322 | -1.0000000 |      -1 | KIN A+  |
|    1329 | 20.4239998 | 1001661 | KIN A+  |
+---------+------------+---------+---------+
11 rows in set (0.05 sec)
```

Figure A.2: Sample MySQL code. This command line selects all runs that had `KIN A+` in their comments, printing the runlength (in minutes) and the number of events in the run. "-1" was the default return value when the information could not be obtained.

Appendix B

Diary

Date	Time	Event
Oct 15	—	Testing starts with runs of cosmics to measure background and to test detectors and software.
Oct 23	15.30	The Pre-beam checklist is gone through by Rusty Salmons. Everything was ok.
Oct 24	17.00	Hall A swept for lock-up.
Oct 25	0.00	The first manned shift.
	20.00	The beam is ready. The commissioning starts with HARP scans and beam position calibrations. Target: BeO.
Oct 26	0.45	Beam centering. Target: Water/No target.
	03.00	Target pump speed calibration. Target: Water.
	07.30	Current scan of target. Target: Water.
	23.00	White spectra for the HRS_r. Target: Water.
Oct 27	05.00	White spectra for the HRS_l. Target: Thick carbon.
	18.20	Optics, ϵ_{coin}, q. Target: Water.
Oct 28	0.00	Target thickness calibration. Target: BeO.
	01.45	Commissioning finished.
	02.15	Kinematics A+. Target: Water.
	13.30	Kinematics G+. Temporary target problems. Target: Water.
Nov 2	02.15	Kinematics F+. Target: Water.
	10.00	BPM calibrations. Arc energy measurement. Target: BeO.
Nov 3	12.30	Kinematics E+. Target: Water.
Nov 4	02.30	Kinematics D+. Target: Water.
	05.30	Kinematics C+. Target: Water.
	12.00	Kinematics B+(1). Problems with target return, but is not discovered. This kinematics was re-done later. Target: Water.
	15.00	Parallel kinematics. Target: Water.
	16.30	Kinematics A–. Target: Water.
	21.45	Kinematics B–. Target: Water.

continued on next page

Date	Time	Event
Nov 5	04.00	Kinematics C–. Target: Water.
	08.45	Kinematics D–. Target: Water.
	13.30	Kinematics I–(1). Target: Water.
	15.30	The CTOF window is reduced from 96 ns to 55 ns.
Nov 6	19.30	Kinematics E–. Target: Water.
Nov 7	01.15	Kinematics F–. Target: Water.
Nov 8	08.15	Kinematics G–. Target: Water.
	10.30	BPM calibration. Target: BeO.
Nov 11	10.30	Kinematics H–(1). Target. Water.
Nov 12	01.00	Parallel kinematics. Target: Water.
	06.00	Kinematics B+(2). Target: Water.
	09.30	Kinematics H+. Target: Water.
Nov 13	19.00	Kinematics I+. Target: Water.
Nov 15	19.00	Parallel kinematics. Target: Water.
	20.30	Kinematics H–(2). Target: Water.
Nov 19	17.45	Kinematics I–(2). Target: Water.
Nov 21	08.00	Beam shutdown for Thanksgiving.
Nov 26	13.00	Pre-beam checklist is gone through by Rusty Salmons.
Nov 28	21.45	Beam is back. Some tests are done to check everything is still ok.
Nov 29	0.30	Kinematics I–(2) continued. Target: Water.
Dec 2	13.30	Parallel kinematics. Target: Water.
	16.00	Kinematics J+. Target: Water.
Dec 4	17.30	Kinematics K+. Target: Water.
	18.00	BCM calibration. Target: Water.
	23.15	Kinematics K+, cont. Target: Water.
Dec 5	14.30	Kinematics G_I^+. Target: Water.
	20.15	Kinematics G+. Target: Water.
	22.15	Kinematics G_{II}^+. Target: Water.
Dec 6	16.00	Hall access to remove target guards and spectrometer caps. They were put on during maintenance Dec 4, but not removed again.
	16.45	Kinematics G_{II}^+, cont. Target: Water.
	21.00	Kinematics G_{II}^-. Target: Water.
Dec 7	11.00	BCM calibration. Target: Water.
	12.30	BPM calibration. Target: Water.
	15.45	Kinematics G_{II}^+, cont. Target: Water.
Dec 8	0.00	Kinematics G_I^-. Target: Water.
	19.45	Parallel kinematics. Target: Water.
	23.00	Target thickness calibration. Target: BeO.
Dec 9	01.00	VDC HV scan.

Appendix C

Corrected Yield Error Estimate

The corrected yield $Y_{\rm cor}$ (the subscript "real" is suppressed in this section for clarity) was defined as

$$Y_{\rm cor} = \left(1 + \frac{Y_{\bar{\rm A}}}{Y_{\rm A}}\right) \cdot \tilde{Y}_{\rm A} \tag{C.1}$$

where $\tilde{Y}_{\rm A}$ was the real yield (from Region A) which belonged to the interval of $E_{\rm miss}$ that was studied, $Y_{\bar{\rm A}}$ was the real yield of all $^{16}{\rm O}(e,e'p)$ channels for -70 MeV $< E_{\rm miss} <$ 150 MeV in Region $\bar{A}$ and $Y_{\rm A}$ was the corresponding yield for Region A. They were in turn defined as

$$\tilde{Y}_{\rm A} = \tilde{Y}_{\rm A,fg} - w \cdot \tilde{Y}_{\rm A,bg} \tag{C.2}$$

$$Y_{\bar{\rm A}} = Y_{\bar{\rm A},{\rm fg}} - 440 \cdot g \tag{C.3}$$

$$Y_{\rm A} = Y_{\rm A,fg} - w \cdot Y_{\rm A,bg} \tag{C.4}$$

where the subscript "fg" indicated foreground yield and "bg" indicated background yield. w $(= w_{\rm fg}/w_{\rm bg})$ was the weight determined by the sizes of the CTOF intervals used. g was the background fit (in events per 0.5 MeV) made to the $E_{\rm miss}$ spectrum and the number 440 came from the fact that the $E_{\rm miss}$ window was 220 MeV wide.

The general formula for estimating the uncertainty in a quantity $f = f(x_1, \ldots, x_n)$ can be written as

$$(\delta f)^2 = \sum_{i=1}^{n} \left[\frac{\partial f}{\partial x_i}\delta x_i\right]^2 \tag{C.5}$$

With $f = Y_{\rm cor}$, the series of terms became

$$\frac{\partial Y_{\rm cor}}{\partial \tilde{Y}_{\rm A,fg}} = 1 + \frac{Y_{\bar{\rm A}}}{Y_{\rm A}}; \tag{C.6}$$

$$\frac{\partial Y_{\rm cor}}{\partial \tilde{Y}_{\rm A,bg}} = -w \cdot \left(1 + \frac{Y_{\bar{\rm A}}}{Y_{\rm A}}\right); \tag{C.7}$$

$$\frac{\partial Y_{\rm cor}}{\partial Y_{\bar{\rm A},{\rm fg}}} = \frac{\tilde{Y}_{\rm A}}{Y_{\rm A}}; \tag{C.8}$$

$$\frac{\partial Y_{\rm cor}}{\partial g} = -440 \cdot \frac{\tilde{Y}_{\rm A}}{Y_{\rm A}}; \tag{C.9}$$

$$\frac{\partial Y_{\rm cor}}{\partial Y_{\rm A,fg}} = -\frac{\tilde{Y}_{\rm A} \cdot Y_{\bar{\rm A}}}{Y_{\rm A}^2}; \tag{C.10}$$

$$\frac{\partial Y_{\rm cor}}{\partial Y_{\rm A,bg}} = w \cdot \frac{\tilde{Y}_{\rm A} \cdot Y_{\bar{\rm A}}}{Y_{\rm A}^2}. \tag{C.11}$$

The uncertainty in each quantity Y is given by $\delta Y = \sqrt{Y}$ while the uncertainty δg in the fit g was given by PAW. Explicitly,

$$Y_{\rm cor} = \left(\tilde{Y}_{\rm A,fg} - w \cdot \tilde{Y}_{\rm A,bg}\right)\left(1 + \frac{Y_{\bar{\rm A},{\rm fg}} - 440 \cdot g}{Y_{\rm A,fg} - w \cdot Y_{\rm A,bg}}\right) \tag{C.12}$$

and

$$\begin{aligned}(\delta Y_{\rm cor})^2 = & \left(1 + \frac{Y_{\bar{\rm A}}}{Y_{\rm A}}\right)^2 \cdot \left(\tilde{Y}_{\rm A,fg} + w^2 \cdot \tilde{Y}_{\rm A,bg}\right) + \\ & + \left(\frac{\tilde{Y}_{\rm A}}{Y_{\rm A}}\right)^2 \cdot \left(Y_{\bar{\rm A},{\rm fg}} + 193600 \cdot (\delta g)^2\right) + \\ & + \left(\frac{\tilde{Y}_{\rm A} \cdot Y_{\bar{\rm A}}}{Y_{\rm A}^2}\right)^2 \left(Y_{\rm A,fg} + w^2 \cdot Y_{\rm A,bg}\right).\end{aligned} \tag{C.13}$$

Equations C.12 and C.13 were used to determined the results presented in Appendix D.

Appendix D

Data subsets

p_{miss} (MeV/c)	Fg	Bg	Sim	RCS	δRCS (%)
66	195 ± 14.0	4 ± 2.0	0.349	336.7 ± 22.3	6.6
68	225 ± 15.0	4 ± 2.0	0.384	352.7 ± 21.7	6.1
70	247 ± 15.7	1 ± 1.0	0.449	332.8 ± 19.4	5.8
72	258 ± 16.1	0 ± 0.0	0.486	321.2 ± 18.3	5.7
74	329 ± 18.1	0 ± 0.0	0.516	385.7 ± 19.5	5.1
76	361 ± 19.0	1 ± 1.0	0.592	369.1 ± 17.8	4.8
78	384 ± 19.6	2 ± 1.4	0.629	369.2 ± 17.3	4.7
80	405 ± 20.1	5 ± 2.2	0.644	379.5 ± 17.4	4.6
82	408 ± 20.2	4 ± 2.0	0.696	353.7 ± 16.1	4.6
84	450 ± 21.2	8 ± 2.8	0.735	369.0 ± 16.0	4.3
86	490 ± 22.1	3 ± 1.7	0.769	385.3 ± 16.0	4.2
88	535 ± 23.1	4 ± 2.0	0.812	398.2 ± 15.8	4.0
90	522 ± 22.8	4 ± 2.0	0.853	369.6 ± 14.9	4.0
92	555 ± 23.6	1 ± 1.0	0.884	379.9 ± 14.8	3.9
94	589 ± 24.3	3 ± 1.7	0.862	413.0 ± 15.6	3.8
96	549 ± 23.4	2 ± 1.4	0.886	374.7 ± 14.7	3.9
98	616 ± 24.8	4 ± 2.0	0.914	407.3 ± 15.1	3.7
100	598 ± 24.5	2 ± 1.4	0.932	388.0 ± 14.6	3.8
102	622 ± 24.9	4 ± 2.0	0.987	380.8 ± 14.0	3.7
104	626 ± 25.0	3 ± 1.7	0.978	386.8 ± 14.2	3.7
106	600 ± 24.5	1 ± 1.0	0.968	374.9 ± 14.0	3.7
108	629 ± 25.1	3 ± 1.7	0.979	388.4 ± 14.2	3.7
110	646 ± 25.4	2 ± 1.4	0.975	400.6 ± 14.5	3.6
112	613 ± 24.8	4 ± 2.0	0.961	385.3 ± 14.3	3.7
114	620 ± 24.9	1 ± 1.0	0.995	377.0 ± 13.9	3.7
116	590 ± 24.3	5 ± 2.2	0.956	372.8 ± 14.1	3.8
118	585 ± 24.2	4 ± 2.0	0.948	373.0 ± 14.2	3.8
120	550 ± 23.5	4 ± 2.0	0.951	349.5 ± 13.7	3.9
122	596 ± 24.4	3 ± 1.7	0.983	366.6 ± 13.8	3.8
124	566 ± 23.8	5 ± 2.2	0.977	349.8 ± 13.5	3.9

continued on next page

p_{miss} (MeV/c)	Fg	Bg	Sim	RCS	δRCS (%)
126	566 ± 23.8	8 ± 2.8	0.966	353.4 ± 13.7	3.9
128	547 ± 23.4	5 ± 2.2	0.955	346.0 ± 13.6	3.9
130	583 ± 24.1	3 ± 1.7	0.929	379.3 ± 14.4	3.8
132	525 ± 22.9	1 ± 1.0	0.954	332.9 ± 13.3	4.0
134	482 ± 22.0	4 ± 2.0	0.969	300.5 ± 12.6	4.2
136	491 ± 22.2	3 ± 1.7	0.932	318.3 ± 13.2	4.1
138	507 ± 22.5	8 ± 2.8	0.929	329.0 ± 13.5	4.1
140	472 ± 21.7	4 ± 2.0	0.908	313.8 ± 13.3	4.2
142	452 ± 21.3	2 ± 1.4	0.937	291.6 ± 12.6	4.3
144	418 ± 20.4	3 ± 1.7	0.909	277.9 ± 12.5	4.5
146	403 ± 20.1	2 ± 1.4	0.870	280.0 ± 12.8	4.6
148	425 ± 20.6	4 ± 2.0	0.913	281.1 ± 12.5	4.5
150	357 ± 18.9	6 ± 2.4	0.908	236.8 ± 11.6	4.9
152	373 ± 19.3	5 ± 2.2	0.905	248.7 ± 11.9	4.8
154	367 ± 19.2	7 ± 2.6	0.875	252.4 ± 12.2	4.8
156	369 ± 19.2	3 ± 1.7	0.877	254.1 ± 12.2	4.8
158	304 ± 17.4	4 ± 2.0	0.852	215.2 ± 11.4	5.3
160	266 ± 16.3	8 ± 2.8	0.866	184.4 ± 10.5	5.7
162	307 ± 17.5	7 ± 2.6	0.819	225.4 ± 11.9	5.3
164	295 ± 17.2	2 ± 1.4	0.837	213.1 ± 11.4	5.4
166	274 ± 16.6	5 ± 2.2	0.803	205.5 ± 11.5	5.6
168	250 ± 15.8	2 ± 1.4	0.802	188.2 ± 10.9	5.8
170	223 ± 14.9	6 ± 2.4	0.783	171.2 ± 10.6	6.2
172	208 ± 14.4	3 ± 1.7	0.798	157.1 ± 10.0	6.4
174	218 ± 14.8	5 ± 2.2	0.767	171.1 ± 10.7	6.3
176	183 ± 13.5	1 ± 1.0	0.734	150.7 ± 10.2	6.8
178	209 ± 14.5	5 ± 2.2	0.747	168.2 ± 10.8	6.4

Table D.1: Relative cross section for kinematics A+. Fg – foreground events; Bg – background events; Sim – phase-space normalisation factor; RCS – relative cross section; δRCS – statistical uncertainty in the relative cross section.

p_{miss} (MeV/c)	Fg	Bg	Sim	RCS	δRCS (%)
111	176 ± 13.3	1 ± 1.0	0.123	375.3 ± 25.8	6.9
113	235 ± 15.3	2 ± 1.4	0.143	430.0 ± 25.6	5.9
115	247 ± 15.7	4 ± 2.0	0.180	359.5 ± 20.9	5.8
117	284 ± 16.9	1 ± 1.0	0.212	351.8 ± 19.0	5.4
119	355 ± 18.8	2 ± 1.4	0.243	383.8 ± 18.6	4.8
121	397 ± 19.9	4 ± 2.0	0.285	365.2 ± 16.7	4.6
123	461 ± 21.5	1 ± 1.0	0.320	378.5 ± 16.0	4.2
125	501 ± 22.4	3 ± 1.7	0.362	363.1 ± 14.8	4.1
127	525 ± 22.9	4 ± 2.0	0.420	327.9 ± 13.0	4.0
129	565 ± 23.8	6 ± 2.4	0.464	319.0 ± 12.3	3.8
131	660 ± 25.7	6 ± 2.4	0.519	333.4 ± 11.8	3.6
133	700 ± 26.5	7 ± 2.6	0.597	307.3 ± 10.6	3.4
135	740 ± 27.2	4 ± 2.0	0.607	320.4 ± 10.7	3.3
137	766 ± 27.7	3 ± 1.7	0.674	298.6 ± 9.8	3.3
139	896 ± 29.9	5 ± 2.2	0.703	334.7 ± 10.2	3.0
141	839 ± 29.0	6 ± 2.4	0.750	293.5 ± 9.2	3.1
143	840 ± 29.0	4 ± 2.0	0.772	285.7 ± 9.0	3.1
145	865 ± 29.4	10 ± 3.2	0.830	273.4 ± 8.5	3.1
147	876 ± 29.6	10 ± 3.2	0.848	270.7 ± 8.4	3.1
149	845 ± 29.1	7 ± 2.6	0.876	253.2 ± 7.9	3.1
151	844 ± 29.1	6 ± 2.4	0.885	250.2 ± 7.9	3.1
153	866 ± 29.4	12 ± 3.5	0.918	247.0 ± 7.7	3.1
155	866 ± 29.4	8 ± 2.8	0.950	239.0 ± 7.4	3.1
157	834 ± 28.9	9 ± 3.0	0.975	224.4 ± 7.1	3.2
159	869 ± 29.5	13 ± 3.6	0.964	236.0 ± 7.3	3.1
161	797 ± 28.2	11 ± 3.3	0.966	216.3 ± 7.0	3.2
163	812 ± 28.5	10 ± 3.2	0.974	218.5 ± 7.0	3.2
165	779 ± 27.9	4 ± 2.0	0.968	211.5 ± 6.9	3.3
167	761 ± 27.6	7 ± 2.6	0.986	202.5 ± 6.7	3.3
169	745 ± 27.3	13 ± 3.6	0.946	206.0 ± 6.9	3.4
171	708 ± 26.6	6 ± 2.4	0.958	193.8 ± 6.6	3.4
173	699 ± 26.4	13 ± 3.6	0.957	191.0 ± 6.6	3.5
175	708 ± 26.6	11 ± 3.3	0.961	192.9 ± 6.6	3.4
177	622 ± 24.9	7 ± 2.6	0.933	174.8 ± 6.4	3.7
179	612 ± 24.7	12 ± 3.5	0.929	172.2 ± 6.4	3.7
181	600 ± 24.5	9 ± 3.0	0.959	163.8 ± 6.1	3.7
183	559 ± 23.6	8 ± 2.8	0.912	160.5 ± 6.2	3.9
185	521 ± 22.8	8 ± 2.8	0.897	152.0 ± 6.1	4.0
187	525 ± 22.9	10 ± 3.2	0.906	151.6 ± 6.1	4.0
189	409 ± 20.2	10 ± 3.2	0.899	118.9 ± 5.4	4.5
191	459 ± 21.4	18 ± 4.2	0.870	137.2 ± 5.9	4.3
193	414 ± 20.3	4 ± 2.0	0.893	121.6 ± 5.5	4.5
195	398 ± 19.9	8 ± 2.8	0.865	120.3 ± 5.5	4.6
197	386 ± 19.6	12 ± 3.5	0.886	113.6 ± 5.3	4.7
199	369 ± 19.2	7 ± 2.6	0.866	111.5 ± 5.3	4.8
201	351 ± 18.7	4 ± 2.0	0.850	108.2 ± 5.3	4.9

continued on next page

p_{miss} (MeV/c)	Fg	Bg	Sim	RCS	δRCS (%)
203	338 ± 18.4	12 ± 3.5	0.829	106.2 ± 5.3	5.0
205	303 ± 17.4	9 ± 3.0	0.843	93.7 ± 4.9	5.3
207	302 ± 17.4	3 ± 1.7	0.815	97.2 ± 5.1	5.3
209	277 ± 16.6	7 ± 2.6	0.805	89.8 ± 4.9	5.5
211	237 ± 15.4	10 ± 3.2	0.765	80.5 ± 4.8	6.0
213	216 ± 14.7	7 ± 2.6	0.767	73.3 ± 4.6	6.3
215	195 ± 14.0	9 ± 3.0	0.753	67.2 ± 4.4	6.6
217	197 ± 14.0	6 ± 2.4	0.726	70.7 ± 4.6	6.5
219	180 ± 13.4	10 ± 3.2	0.700	66.6 ± 4.6	6.9

Table D.2: Relative cross section for kinematics C+. Fg – foreground events; Bg – background events; Sim – phase-space normalisation factor; RCS – relative cross section; δRCS – statistical uncertainty in the relative cross section.

p_{miss} (MeV/c)	Fg	Bg	Sim	RCS	δRCS (%)
153	237 ± 15.4	1 ± 1.0	0.291	243.6 ± 16.2	6.6
155	263 ± 16.2	6 ± 2.4	0.327	239.4 ± 15.1	6.3
157	270 ± 16.4	5 ± 2.2	0.390	206.3 ± 12.7	6.1
159	302 ± 17.4	5 ± 2.2	0.430	209.8 ± 12.2	5.8
161	339 ± 18.4	4 ± 2.0	0.463	218.6 ± 12.0	5.5
163	333 ± 18.2	6 ± 2.4	0.533	186.4 ± 10.2	5.5
165	349 ± 18.7	3 ± 1.7	0.566	184.2 ± 9.8	5.3
167	405 ± 20.1	1 ± 1.0	0.620	195.8 ± 9.7	5.0
169	429 ± 20.7	7 ± 2.6	0.652	196.3 ± 9.5	4.8
171	429 ± 20.7	8 ± 2.8	0.699	183.1 ± 8.8	4.8
173	436 ± 20.9	12 ± 3.5	0.769	168.5 ± 8.0	4.8
175	426 ± 20.6	2 ± 1.4	0.777	164.2 ± 7.8	4.8
177	457 ± 21.4	10 ± 3.2	0.839	162.2 ± 7.5	4.6
179	430 ± 20.7	4 ± 2.0	0.871	147.7 ± 7.0	4.7
181	434 ± 20.8	11 ± 3.3	0.900	143.5 ± 6.8	4.7
183	439 ± 21.0	10 ± 3.2	0.909	143.8 ± 6.7	4.7
185	408 ± 20.2	10 ± 3.2	0.906	134.0 ± 6.5	4.8
187	400 ± 20.0	7 ± 2.6	0.966	123.5 ± 6.0	4.9
189	383 ± 19.6	11 ± 3.3	0.979	116.3 ± 5.8	5.0
191	402 ± 20.0	8 ± 2.8	0.963	124.4 ± 6.0	4.8
193	372 ± 19.3	6 ± 2.4	0.981	113.1 ± 5.7	5.0
195	369 ± 19.2	12 ± 3.5	0.981	111.8 ± 5.6	5.0
197	351 ± 18.7	8 ± 2.8	0.982	106.4 ± 5.5	5.1
199	345 ± 18.6	8 ± 2.8	0.985	104.2 ± 5.4	5.2
201	329 ± 18.1	12 ± 3.5	1.000	97.6 ± 5.2	5.3
203	328 ± 18.1	10 ± 3.2	0.967	100.8 ± 5.4	5.3
205	292 ± 17.1	7 ± 2.6	0.989	87.9 ± 4.9	5.6

continued on next page

p_{miss} (MeV/c)	Fg	Bg	Sim	RCS	δRCS (%)
207	284 ± 16.9	7 ± 2.6	0.983	86.0 ± 4.9	5.7
209	287 ± 16.9	6 ± 2.4	0.972	88.0 ± 5.0	5.6
211	262 ± 16.2	10 ± 3.2	0.934	83.2 ± 4.9	5.9
213	260 ± 16.1	7 ± 2.6	0.971	79.7 ± 4.7	5.9
215	238 ± 15.4	3 ± 1.7	0.949	74.9 ± 4.6	6.1
217	197 ± 14.0	10 ± 3.2	0.938	62.0 ± 4.2	6.8
219	187 ± 13.7	5 ± 2.2	0.911	61.0 ± 4.2	6.9
221	207 ± 14.4	11 ± 3.3	0.912	67.0 ± 4.4	6.6
223	209 ± 14.5	8 ± 2.8	0.896	69.2 ± 4.6	6.6

Table D.3: Relative cross section for kinematics D+. Fg – foreground events; Bg – background events; Sim – phase-space normalisation factor; RCS – relative cross section; δRCS – statistical uncertainty in the relative cross section.

p_{miss} (MeV/c)	Fg	Bg	Sim	RCS	δRCS (%)
172	186 ± 13.6	3 ± 1.7	0.103	166.0 ± 11.1	6.7
176	254 ± 15.9	3 ± 1.7	0.169	138.5 ± 7.9	5.7
180	338 ± 18.4	13 ± 3.6	0.219	141.5 ± 7.1	5.0
184	442 ± 21.0	5 ± 2.2	0.295	138.2 ± 6.0	4.3
188	523 ± 22.9	6 ± 2.4	0.377	127.8 ± 5.1	4.0
192	569 ± 23.9	17 ± 4.1	0.467	111.7 ± 4.3	3.8
196	603 ± 24.6	10 ± 3.2	0.549	101.2 ± 3.8	3.7
200	631 ± 25.1	19 ± 4.4	0.659	87.8 ± 3.2	3.6
204	649 ± 25.5	24 ± 4.9	0.744	79.9 ± 2.9	3.6
208	683 ± 26.1	15 ± 3.9	0.821	76.6 ± 2.7	3.5
212	636 ± 25.2	22 ± 4.7	0.881	66.1 ± 2.4	3.6
216	609 ± 24.7	23 ± 4.8	0.912	61.1 ± 2.3	3.7
220	573 ± 23.9	26 ± 5.1	0.959	54.6 ± 2.1	3.8
224	583 ± 24.1	19 ± 4.4	0.978	54.7 ± 2.1	3.8
228	517 ± 22.7	23 ± 4.8	0.976	48.4 ± 2.0	4.0
232	397 ± 19.9	29 ± 5.4	1.000	36.0 ± 1.7	4.7
236	389 ± 19.7	29 ± 5.4	0.987	35.7 ± 1.7	4.7
240	367 ± 19.2	22 ± 4.7	0.977	34.2 ± 1.6	4.8
244	321 ± 17.9	22 ± 4.7	0.956	30.5 ± 1.6	5.2
248	276 ± 16.6	15 ± 3.9	0.923	27.3 ± 1.5	5.6
252	251 ± 15.8	19 ± 4.4	0.907	25.1 ± 1.5	5.9
256	217 ± 14.7	17 ± 4.1	0.847	23.2 ± 1.5	6.3
260	186 ± 13.6	24 ± 4.9	0.835	19.9 ± 1.4	6.9

Table D.4: Relative cross section for kinematics E+. Fg – foreground events; Bg – background events; Sim – phase-space normalisation factor; RCS – relative cross section; δRCS – statistical uncertainty in the relative cross section.

p_{miss} (MeV/c)	Fg	Bg	Sim	RCS	δRCS (%)
241	215 ± 14.7	17 ± 4.1	0.148	22.8 ± 1.58	6.9
245	268 ± 16.4	17 ± 4.1	0.200	21.1 ± 1.29	6.1
249	351 ± 18.7	25 ± 5.0	0.259	21.3 ± 1.14	5.4
253	399 ± 20.0	45 ± 6.7	0.336	18.4 ± 0.93	5.0
257	403 ± 20.1	45 ± 6.7	0.417	15.0 ± 0.74	5.0
261	436 ± 20.9	65 ± 8.1	0.490	13.7 ± 0.66	4.8
265	431 ± 20.8	61 ± 7.8	0.595	11.1 ± 0.53	4.8
269	473 ± 21.7	71 ± 8.4	0.687	10.6 ± 0.48	4.6
273	428 ± 20.7	85 ± 9.2	0.761	8.5 ± 0.41	4.8
277	469 ± 21.7	105 ± 10.2	0.820	8.6 ± 0.40	4.7
281	420 ± 20.5	99 ± 9.9	0.885	7.1 ± 0.35	4.9
285	407 ± 20.2	110 ± 10.5	0.911	6.6 ± 0.33	5.0
289	395 ± 19.9	104 ± 10.2	0.950	6.2 ± 0.31	5.1
293	382 ± 19.5	112 ± 10.6	0.968	5.8 ± 0.30	5.2
297	375 ± 19.4	97 ± 9.8	0.979	5.7 ± 0.30	5.2
301	319 ± 17.9	99 ± 9.9	0.991	4.7 ± 0.27	5.7
305	340 ± 18.4	114 ± 10.7	0.963	5.1 ± 0.29	5.6
309	287 ± 16.9	99 ± 9.9	0.976	4.3 ± 0.26	6.1
313	267 ± 16.3	96 ± 9.8	0.932	4.1 ± 0.26	6.4
317	268 ± 16.4	101 ± 10.0	0.884	4.3 ± 0.28	6.4

Table D.5: Relative cross section for kinematics F+. Fg – foreground events; Bg – background events; Sim – phase-space normalisation factor; RCS – relative cross section; δRCS – statistical uncertainty in the relative cross section.

Bibliography

[1] H. Palevsky et al. Elastic scattering of 1-BeV protons from hydrogen, helium, carbon, and oxygen nuclei. *Phys. Rev. Lett.*, 18:1200, 1967.

[2] J. M. Cameron, J. R. Richardson, W. T. H. van Oers, and J. W. Verba. Studies of the energy dependence of p-O^{16} interactions between 20 and 50 MeV. I. Measurements of the differential cross sections of protons elastically scattered by O^{16} at 23.4, 24.5, 27.3, 30.1, 34.1, 36.8, 39.7, 43.1, and 46.1 MeV. *Phys. Rev.*, 167:908, 1968.

[3] H. B. Eldridge, S. N. Bunker, J. M. Cameron, and J. R. Richardson. Studies of the energy dependence of p-O^{16} interactions between 20 and 50 MeV. II. Measurements of the polarization of protons elastically scattered by O^{16} at 24.5, 27.3, 30.1, 34.1, 36.8, and 39.7 MeV. *Phys. Rev.*, 167:915, 1968.

[4] G. S. Adams et al. Microscopic description of 800-MeV polarized-proton scattering from ^{16}O. *Phys. Rev. Lett.*, 43:421, 1979.

[5] P. Schwandt et al. Analyzing power of proton-nucleus elastic scattering between 80 and 180 MeV. *Phys. Rev. C*, 26:55, 1982.

[6] R. W. Fergerson et al. Spin-rotation parameter Q for 800 MeV proton elastic scattering from ^{16}O, ^{40}Ca, and ^{208}Pb. *Phys. Rev. C*, 33:239, 1986.

[7] E. Bleszynski et al. Energy dependence of relativistic effects in the elastic scattering of polarized protons from ^{16}O and ^{40}Ca. *Phys. Rev. C*, 37:1527, 1988.

[8] Z.-Q. Tan and W.-Y. Ruan. Proton-oxygen elastic scattering and spin effects at $T_p = 200$ MeV in the four α-particle model. *Nucl. Part. Phys.*, 15:1599, 1989.

[9] J. J. Kelly et al. Effective interactions and nuclear structure using 180 MeV protons. i. $^{16}\mathrm{O}(p,p')$. *Phys. Rev. C*, 41:2504, 1990.

[10] J. J. Kelly et al. Effective interaction for $^{16}\mathrm{O}(p,p')$ at $E_p = 318$ MeV. *Phys. Rev. C*, 43:1272, 1991.

[11] H. Seifert et al. Effective interaction for $^{16}\mathrm{O}(p,p')$ and $^{40}\mathrm{Ca}(p,p')$ at $E_p = 200$ MeV. *Phys. Rev. C*, 47:1615, 1993.

[12] M. N. Rosenbluth. High energy elastic scattering of electrons on protons. *Phys. Rev.*, 79:615, 1950.

[13] K. G. Fissum et al. The dynamics of the quasielastic ^{16}O$(e,e'p)$ reaction at $Q^2 = 0.8$ (GeV/c)^2. *Phys. Rev. C*, 70:034606, 2004.

[14] M. Leuschner et al. Quasielastic proton knockout from ^{16}O. *Phys. Rev.*, C49:955, 1994.

[15] C. M. Spaltro et al. Separated structure functions for the proton-knockout reaction ^{16}O$(e,e'p)$. *Phys. Rev.*, C48:2385, 1993.

[16] L. Chinitz et al. Separation of the Interference Response Function $R_{\rm LT}$ in the ^{16}O$(e,e'p)^{15}$N Reaction. *Phys. Rev. Lett.*, 67:568, 1991.

[17] M. Bernheim. The influence of bound state and optical potentials on 1p momentum distributions obtained from ^{12}C and ^{16}O$(e,e'p)$ reactions. *Nucl. Phys.*, A375:381, 1982.

[18] K. I. Blomqvist et al. High-momentum components in the $1p$ orbitals of ^{16}O. *Phys. Lett.*, B344:85, 1995.

[19] J. Gao et al. Dynamical relativistic effects in quasielastic $1p$-shell proton knockout from ^{16}O. *Phys. Rev. Lett.*, 84:3265, 2000.

[20] N. Liyanage et al. Dynamics of the ^{16}O$(e,e'p)$ Reaction at High Missing Energies. *Phys. Rev. Lett.*, 86:5670, 2001.

[21] J. Alcorn et al. Basic instrumentation for hall a at Jefferson Lab. To be published.

[22] K. G. Fissum et al. Vertical drift chambers for the Hall A high-resolution spectrometers at Jefferson Lab. *Nucl. Instr. Meth. in Phys. Res.*, A474:108, 2001.

[23] A. Saha et al. Testing the Limits of the Single Particle Model in ^{16}O$(e,e'p)$: An Update to E89-003. JLAB PAC 18, May 2000.

[24] `http://www.jlab.org/~luminita/vcs.html`.

[25] S. Jaminion and H. Fonvieille. Y_{target} optimization for E93050 experiment. Technical report, VCS Collaboration, 1998.

[26] K. Fissum and P. Ulmer. Systematic uncertainties in E89-003. Technical Report JLAB-TN-02-015, Hall A Collaboration, 2002.

[27] M. M. Sharma, M. A. Nagarajan, and P. Ring. Rho meson coupling in the relativistic mean field theory and description of exotic nuclei. *Phys. Lett. B*, 312:377, 1993.

[28] M. Gari and W. Krümpelmann. Semiphenomenological synthesis of meson and quark dynamics and the electromagnetic structure of the nucleon. *Z. Phys. A*, 322:689, 1985.

[29] T. de Forest, Jr. Off-shell electron-nucleon cross sections : The impulse approximation. *Nucl. Phys.*, A392:232, 1983.

[30] E. D. Cooper, S. Hama, B. C. Clark, and R. L. Mercer. Global Dirac phenomenology for proton-nucleus elastic scattering. *Phys. Rev. C*, 47:297, 1993.

[31] J. M. Udías. Private communication.